Air plasma sprayed multi-material composite coatings for enhanced light absorption and thermal emission.

FAISAL, N.H., RAJENDRAN, V., KANIAPAN, S., RAMALINGAM, V., PRATHURU, A., AHMED, R., KATIYAR, N.K., BANSAL, A., WHITTAKER, T., ISHERWOOD, P., WHITTOW, W., EGIZA, M. and GOEL, S.

2025

Air plasma sprayed multi-material composite coatings for enhanced light absorption and thermal emission

Nadimul Haque Faisal [a,*], Vinooth Rajendran [a], Siva Kaniapan [a], Vinoth Ramalingam [a], Anil Prathuru [a], Rehan Ahmed [b], Nirmal Kumar Katiyar [c], Aakash Bansal [d], Thomas Whittaker [d], Patrick Isherwood [d], Will Whittow [d], Mohamed Egiza [a,e], Saurav Goel [f,g]

[a] School of Computing, Engineering and Technology, Robert Gordon University, Garthdee Road, Aberdeen AB10 7GJ, UK
[b] School of Engineering and Physical Sciences, Heriot-Watt University, Edinburgh EH14 4AS, UK
[c] Amity Institute of Applied Sciences, Amity University, Noida 201303, India
[d] Wolfson School of Mechanical, Electrical and Manufacturing Engineering, Loughborough University, Loughborough LE11 3TU, UK
[e] Department of Mechanical Engineering, Kafrelsheikh University, Kafrelsheikh 33516, Egypt
[f] School of Engineering, London South Bank University, 103 Borough Road, London SE1 0AA, UK
[g] Department of Mechanical Engineering, University of Petroleum and Energy Studies, Dehradun 248007, India

ARTICLE INFO

ABSTRACT

This study pioneers a transformative approach to solar thermal technology by leveraging air plasma-sprayed (APS) multi-material composite coatings. It is to achieve unprecedented light absorption and thermal emission, redefining the design paradigm for bi-layer coatings in solar thermal applications. For the first time, both single-layer (Mo-Mo$_2$C/ceramic, NiO/YSZ) and bi-layer (NiO/YSZ with an additional 8YSZ top layer) coatings on Hastelloy®X substrate were systematically compared using an extensive suite of characterisation techniques, including scanning electron microscopy (SEM), energy-dispersive X-ray spectroscopy (EDS), X-ray diffraction (XRD), optical spectroscopy, infrared thermography, surface roughness, sheet resistance, electrical conductivity, dielectric constant measurements and water absorbency tests. The bi-layer NiO/YSZ + 8YSZ coating with the highest surface roughness demonstrated remarkable light absorption and thermal emission properties. With a minimal light reflectance of 0.1 and a high thermal emittance of 0.961, this configuration achieved superior solar energy capture and efficient heat re-emission, outperforming single-layer coatings with a moderate reflectance of 0.2 to 0.6. Additionally, the Mo-Mo$_2$C/ZrO$_2$ coating revealed unique spectral behavior with enhanced reflectance in the infrared region, indicating its potential for niche applications. Moreover, the NiO/YSZ + 8YSZ and NiO/YSZ coatings configuration also exhibited minimal water absorbency due to its fine microstructure, characterised by small pore sizes and low surface-connected porosity. These findings establish the bi-layer NiO/YSZ + 8YSZ coating as a groundbreaking advancement in thermal-sprayed materials, offering exceptional solar selective and thermal emission properties. This work underscores the transformative potential of APS techniques in developing next-generation coatings tailored for optimised solar thermal applications.

1. Introduction

Solar selective and thermal emission coating materials can be developed to control the absorption and emission of energy in solar thermal and other energy applications. While the solar selective coating materials are typically used to absorb solar radiation and minimise heat loss due to infrared (IR) emission, whereas thermal emission coating materials are typically developed to control the radiation of heat from a surface. Their performance is generally based on their ability to optimise how the material's surface interacts with the electromagnetic spectrum, particularly sunlight and thermal infrared radiation, and the dual functionality of coating materials could be critical in advancing technologies for sustainable energy and thermal management. This study investigates the light absorption and thermal emission performance of various coating materials developed using air plasma spray (APS) technique. Here, the coatings are developed by combining multi-

---

materials, leveraging their synergistic properties to achieve desired optical and thermal characteristics.

Specialised coatings play a crucial role in enhancing solar radiation absorption by minimising surface reflection in selective absorbers [1]. Antireflective coatings can be developed through various strategies, such as using materials with an intermediate refractive index (RI) between the substrate and air, incorporating porosity, employing graded refractive indices, or combining these approaches [2]. Common dielectric materials with intermediate RI values suitable for such applications include alumina (Al_2O_3, RI ~ 1.65), titania (TiO_2, RI ~ 2.30) [3], zirconia (ZrO_2, RI ~ 2.14–2.08) [4], nickel oxide (NiO, RI ~ 2.18) [5], and 8 mol% yttria-stabilized zirconia (8YSZ, RI ~ 2.20) [6]. Various coating techniques, such as chemical vapor deposition (CVD), spray coating, spin coating, dip coating, electroless plating, electroplating, sputtering, and sol-gel processing, have been employed for different applications [7], each offering unique advantages and challenges in tailoring coating properties for specific requirements.

Thermally sprayed coatings offer the flexibility to engineer specific microstructures, enabling tailored antireflection properties ideal for manufacturing selective absorber surfaces [7,8]. Recent reviews [9] highlight numerous applications where thermal spray techniques have been employed to create coatings capable of absorbing and shielding non-ionising electromagnetic (EM) waves across a broad spectrum, including microwave, millimeter-wave, solar selective, photocatalytic, interference shielding, and thermal barrier applications. These coatings can incorporate diverse structural features such as elastic frameworks, cavities, porosities, voids, and cracks, which can be strategically designed for enhanced performance in various industrial contexts [10–13]. Engineered porosities and cavities, in particular, play a critical role in optimizing material absorption properties, leveraging the intrinsic advantages of thermal spray processes [14]. However, for heterogeneous materials, the complex interactions involving EM wave scattering and absorption present significant challenges to predict and optimise, requiring further investigation.

Extensive literature demonstrates that solar selective coatings can be effectively manufactured using thermal spray techniques, such as air plasma spray (APS) and high-velocity oxy-fuel (HVOF) [15–21]. Using the plasma spray method, Tului et al. (2004) [15] deposited ZnO and ZnO + (3 wt% and 22 wt%) Al_2O_3 material onto the sand-blasted steel substrates and reported the optical and thermal properties. While the coatings containing 22 wt% of Al_2O_3 showed lower emissivity in the visible range than the corresponding 3 wt% Al_2O_3 containing coatings, it was also demonstrated that the infrared (IR) emissivity of thermally sprayed coatings can depend on a range of factors, such as the wavelength, chemical composition, and the spraying environment. Using the suspension plasma spray (SPS) method, Vaßen et al. (2009) [16] deposited porous TiO_2 coatings onto indium tin oxide (ITO) coated glass substrates for photovoltaic cells, and through analysis of photovoltaic current-voltage (I-V) curves, they identified coatings with the best optical properties to those containing 90 % anatase phase.

Using a HVOF spray method, Gao et al. (2015) [17] deposited 30 μm thick Ni—Mo and Ni-Mo-Co onto the 307 L stainless steel substrates. To improve the solar spectral absorption for concentrating solar power applications (in the spectral range ~ 0.3–2.5 μm), the coatings were irradiated using the laser treatment. Influencing the phase content and making the coating denser by significantly reducing micropores. For as-sprayed samples, it was observed that coatings had undesirable surface-connected micro-pores. Reflectance curves showed enhanced solar absorbing properties (about 10.7 % increase in solar absorptance) on the laser-treated coatings compared to the as-sprayed coatings. Using the HVOF spray method, Wang et al. (2017) [18] investigated 45 μm thick tungsten carbide/cobalt (WC/Co) coatings on AISI 304 L stainless steel substrates. Analysis showed that the multimodal WC/Co coating with coarse and fine WC particles exhibited a higher solar absorptance (0.87) than what was achieved by either coarse powders (0.80) or fine powders (0.82) alone. Higher solar absorbance was attributed to the formation of

a dense layer with no decarburised phases and distributed WC particles.

Duan et al. (2017) [19] proposed an innovative method to deposit a duplex layer of coatings. This included a first layer deposition of Co-WC-Al_2O_3 (absorbing layer deposited using the HVOF method) followed by an Al_2O_3 (antireflection layer deposited using the sol-gel method) ceramic metal-dielectric. Analysis showed that the duplex coating exhibited high solar absorptance/emittance (0.908/0.145). However, after annealing, the absorptance/emittance decreased to 0.898/0.172, an indication of the thermally stable characteristics of the coating. Similarly, using an HVOF method, Ke et al. (2018) [20] deposited 45 μm thick WC-Co coatings on the stainless-steel substrates. Then, they included layers of coatings ($CuCoMnO_x$, $CuCoMnO_x$-SiO_2, and SiO_2 sols) synthesised by a sol-gel method and deposited successively on the coating. Multilayers of $CuCoMnO_x$ and $CuCoMnO_x$-SiO_2 were used as sealing layers to fill larger and smaller pores, followed by the uppermost SiO_2 antireflective layer. Analysis showed that the absorptance increased from 0.821 to 0.915 and the emittance decreased from 0.434 to 0.290, and after annealing of coating, the absorption and emittance of the multilayered coatings changed to 0.901/0.320. Deng et al. (2020) [21] studied vanadium tailings deposited on a stainless-steel substrate with a Ni/Al bond layer using the plasma spraying method, and the analysis exhibited high absorbance (93.79 %) and low-energy band gaps, emissivity of 71 % at 120 °C, and high thermal stability at 500 °C. Whilst there are multiple advantages in using multi-material coatings for electromagnetic wave absorption (e.g., ultraviolet-visible-infrared (UV–Vis-IR) spectral range), the design of materials and surface manufacturing can be complex. It may require sophisticated manufacturing techniques such as thermal spray coatings.

The selection of multi-material coatings is driven by the specific requirements, manufacturability, and constraints of the application. These coatings are engineered by combining two or more materials to enhance desirable properties. For example, Mo-Mo_2C composites show enhanced photo-absorption in the 200 nm to 800 nm wavelength range [22] and Mo_2C (a transition metal/metal-carbide composite) has notable opto-electrical characteristics, making it suitable for applications in semi-conductor photonics [23]. Mo_2C is promising for use in optically activated thermal switches, energy storage, adsorption, and optoelectronic sensors [24]. To broaden Mo_2C's application in semiconductor optoelectronics and optimise its activity, selectivity, and carbide formation, adding metal oxides is a viable strategy. Metal oxides, known for their high thermal stability and wide range of band gaps, can be tailored to absorb specific regions of the electromagnetic spectrum. For instance, aluminum oxide (Al_2O_3, with a band gap of ~6 eV) is used in optical coatings for the near-UV to IR regions, titanium oxide (TiO_2, with a band gap of ~3.4–3.6 eV) is used in the visible range, and zirconium oxide (ZrO_2, with a band gap of ~5 eV) is suitable for near-UV to IR coatings but does not absorb sunlight effectively, as it only captures ultraviolet light [25].

Similarly, materials like nickel oxide (NiO) and yttria-stabilized zirconia (YSZ) are refractory materials with high thermal stability, making them ideal for solar thermal applications. NiO, with a band gap of 3.6 eV to 4.0 eV, can absorb a wide range of wavelengths, while YSZ (with a band gap of 5.0 eV to 5.2 eV) offers high ionic conductivity at elevated temperatures, especially at 8YSZ, along with excellent thermal stability and low thermal conductivity [26,27]. The combination of NiO's high light absorption in the ultraviolet to visible spectrum and electronic conductivity with YSZ's thermal stability, low thermal conductivity, and ionic conductivity creates a synergistic system ideal for efficient heat and charge transfer. This combination of properties can enhance light absorption and thermal emission for applications in solar energy conversion.

This study investigates the performance of five thermally sprayed coatings—four single-layer systems (Mo-Mo_2C/Al_2O_3, Mo-Mo_2C/ZrO_2, Mo-Mo_2C/TiO_2, NiO/YSZ) and one bi-layer system (8YSZ coated onto NiO/YSZ) - deposited on Hastelloy®X substrates. The coatings were rigorously evaluated for their potential in efficient solar energy

conversion, with a focus on their microstructure, sheet resistance, conductivity, dielectric properties, optical and thermal performance, and water absorbency.

2. Materials and methods

2.1. Material selection

Hastelloy®X (nickel-chromium-iron-molybdenum alloy) was chosen as a substrate as it has good oxidation resistance and high-temperature strength. Mo with Mo_2C (i.e., Mo-Mo_2C; average particle size distribution of 35–40 μm) (Metco 64) powder was chosen for the coating. It was sintered spheroidal powder, demonstrating high scuff resistance, frictional characteristics, and toughness. Al_2O_3 powder with an average particle size distribution of 35–50 μm (METCO-105SFP) was chosen. The powder was fused and crushed with angular and blocky morphology, demonstrating wear-resistant properties, including chemical inertness and stability at high temperatures. ZrO_2 with an average particle size distribution of 100–120 μm (40,453, Alfa Aesar) was chosen as fused and crushed, demonstrating stability in oxidising and reducing atmospheres. TiO_2 with average particle size distribution of 32–40 μm (METCO-6231A) was chosen as fused, crushed, agglomerated, and sintered with angular, blocky, or spheroidal powder, which demonstrates low electrical resistivities and superior tribological properties. Nanostructured NiO/YSZ powder containing 50 wt% each with an average granule size of 30–40 μm (Nanox™ S28ZY8; Inframat®) was chosen as an agglomerated composite with spherical granule morphology.

2.2. Coating preparation

In this study, a single-layer coating consists of a single material composition applied to a substrate, while a bi-layer coating features two distinct layers, each made from different materials, with each layer serving a specific function to improve overall performance. The processing parameters, namely angle, current, hydrogen flow, spray distance and feed rate, were identified for effective air plasma spraying (APS) onto the Hastelloy®X disc (20 mm diameter and 4.76 mm thickness) as shown in Table 1. Various coatings were disposed of at an

industrial facility (Monitor Coating Limited, UK) using industrially optimised process parameters of the APS system (Metco 3 MB gun, 3M7A-GP nozzle, Metco).

2.3. Characterisation

2.3.1. Microstructural characterisation

Scanning electron microscope (SEM) from Karl Zeiss EVO LS10 and JEOL JSM 6010 LA was used to analyse the coating morphology (on the surface, whereas the chemical elemental analysis (Energy Dispersive X-ray Spectrometer or EDS) was done using Karl Zeiss EVO LS10 electron microscope. The phase of coated materials was analysed using an X-ray diffractometer (Bruker D8 Focus) with Cu K-α radiation ($l = 0.154$ nm; step size 0.02°). The surface roughness (centre line average, R_a) of samples were measured by Taylor Hobson (Surtronic 3+) tester. On each sample, three roughness measurements were taken at different locations with sampling length of 2.5 mm and an evaluation length of 12.5 mm.
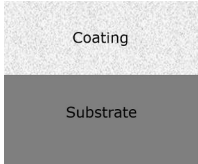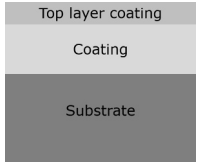
2.3.2. Sheet resistance and electrical conductivity

The 4-point probe method [28] was used to analyse the sample's sheet resistance and electrical conductivity. Sheet resistance (or surface resistance) is a measure of lateral resistance per square area of coating with uniform thickness, and demonstrate the ability of an electrical charge to travel in the plane of the coating layer. The 4-point probe measurement system manufactured by Ossila B*V* (The Netherlands) was used. It operates in the range of ±100 μV to ±10 V, ±1 μA to ±200 mA current range, and 100 mΩ/square to 10 MΩ/square sheet resistance range.

2.3.3. Dielectric constant measurements

The dielectric constant (relative permittivity) was measured with the capacitance generated by the coating when placed between the two conducting plates. It measures how much a material can be polarised by an electric field relative to a vacuum and demonstrates the ability to store electrical energy. In this experiment, the conductive substrate was used as one plate, and a copper sheet of radius 9.9 mm and thickness 0.03 mm was used as the second plate placed on top of the coating, as per the scheme shown in Fig. 1. An LCR meter was used to measure the

Table 1
Air plasma spray process parameters used for coating manufacturing.

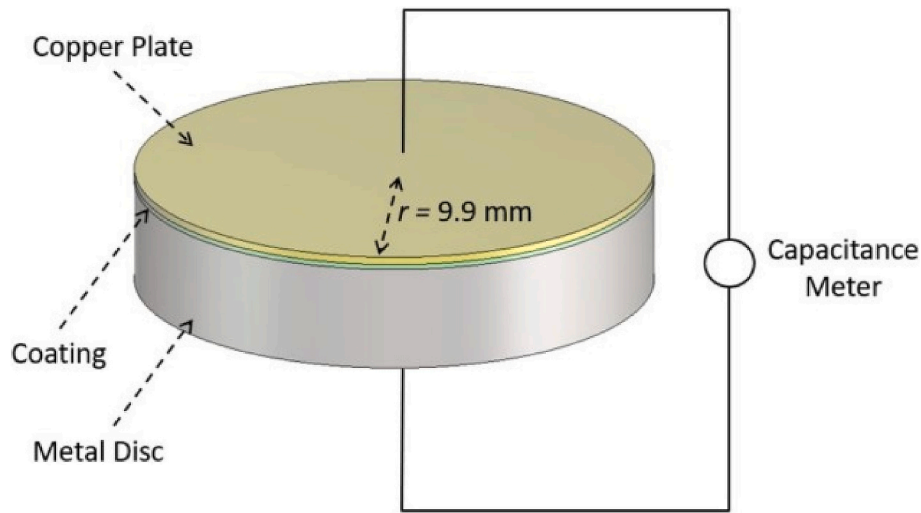| Materials deposited using air plasma spraying (APS) technique (9 MB, Sulzer Metco)					
Materials	(a)	(b)	(c)	(d)	(e)
Feedstock materials	Mo-Mo_2C:Al_2O_3 (wt % ratio of 80:20)	Mo-Mo_2C:TiO_2 (wt % ratio of 80:20)	Mo-Mo_2C:ZrO_2 (wt % ratio of 80:20)	NiO/YSZ (wt% ratio of 50:50)	NiO/YSZ (wt% ratio of 50:50) and top layer 8%mol YSZ
Coating-substrate system (single layer, duplex or bi-layer)	(Single-layer coating)				(Bi-layer coating)
Coating thickness	250 μm (Mo-Mo_2C/Al_2O_3)	300 μm (Mo-Mo_2C/TiO_2)	220 μm (Mo-Mo_2C/ZrO_2)	250 μm (NiO/YSZ)	Total 300 μm (50 μm 8%mol YSZ top layer coating on top of 250 μm thick NiO/YSZ)
Substrate	Hastelloy®X (20 mm diameter, 4.76 mm thickness)				
Air plasma spray process parameters					
Voltage	69 *V*			55 V	
Current	500 A			700 A	
Primary gas (Ar) flow	0.68 MPa; 42.08 lpm			0.68 MPa; 47.1 lpm	
Auxiliary/secondary gas (H_2) flow	0.34 MPa; 34.2 lpm			0.4 MPa; 12.5 lpm	
Carrier (Ar) gas flow	0.68 MPa; 19.4 lpm			–	
Spray distance	100 mm			100 mm	
Transverse speed	30 mm/s			30 mm/s	
Feed rate	70 g/m			66 g/m	33 g/m
Angle (°)	30°			30°	

Fig. 1. Capacitance measurement scheme for the coating-substrate system (measured for NiO/YSZ and NiO/YSZ + 8YSZ coatings, as other coatings were conductive).

capacitance at 1 kHz. The measured capacitance was used to calculate the relative permittivity of the material using Eq. (1):

$$\varepsilon_r = \frac{C\,d}{\pi r^2 \varepsilon_0} \tag{1}$$

where C is the measured capacitance, d is the coating thickness, r is the radius of the substrate cylinder, and ε_0 is the absolute permittivity of free space.

2.3.4. Spectroscopy analysis

2.3.4.1. UV–vis-IR spectroscopy. The UV–Vis-IR spectroscopy measurement was performed using a Perkin Elmer Lambda 900 spectrophotometer (near normal incidence = 6° (unpolarised light)) in reflectance mode in the wavelength range of 300 nm and 2000 nm in steps of 2 nm.

2.3.4.2. Optical band gap energy determination. The optical band gap of the materials can be estimated from the Tauc plot [29] obtained from the data based on Eq. (2) [30]:

$$(\alpha.h\nu)^{1/\gamma} = B(h\nu - E_g) \tag{2}$$

where α is the wavelength-dependent absorption coefficient, h is Planck's constant, ν is the photon frequency, E_g is the band gap energy, and B is a constant. The γ factor depends on the nature of the electron transition and is equal to 1/2 for the indirect and 2 for direct transition band gaps. The band gap energy is usually determined from diffuse reflectance spectra. According to the theory of Kubelka and Munk (1931) [31], the measured reflectance spectra can be transformed to the corresponding absorption spectra by applying the Kubelka–Munk function ($F(R_\infty)$), eq. (3).

$$F(R_\infty) = \frac{K}{S} = \frac{(1 - R_\infty)^2}{2R_\infty} \tag{3}$$

where $R_\infty = \frac{R_{sample}}{R_{standard}}$ is the reflectance of an infinitely thick specimen, while K and S are the absorption and scattering coefficients, respectively. Substituting $F(R_\infty)$ for α in Eq. (2) yields Eq. (4):

$$(F(R_\infty).h\nu)^{1/\gamma} = B(h\nu - E_g) \tag{4}$$

2.3.4.3. Emittance calculation in the solar spectrum. As per the mechanism of spectral selectivity [7], the spectral range of solar radiation is very wide. While the energy is mainly concentrated in the range of Vis- and near-IR spectrum, the wavelength of thermal radiation of the absorber is >2.5 μm. Emissivity (a material property which measures the efficiency with which the body emits energy, and measures only the intensity of thermal radiation) is the measure of an object's ability to emit any energy within the electromagnetic spectrum (and it is a dimensionless number between 0 (for a perfect reflector) and 1 (for a perfect emitter)). The emittance (ε) (a measurable physical quantity which measures the amount of energy emitted per unit area, may include radiant energy emitted from Vis-, IR or UV-light) is the ratio of the radiation emitted at a given temperature to the radiation emitted by a perfect blackbody at the same temperature [7,21]. From the measured spectral reflectance, average emittance (ε) of the sample can be calculated (integrated here over the solar spectrum) according to Eq. (5) [7,21].

$$\varepsilon_{therm}(T) = \frac{\int_{300nm}^{2000nm} (1 - \rho(\lambda))P_b(\lambda, T)\partial\lambda}{\int_{300nm}^{2000nm} P_b(\lambda, T)\partial\lambda} \tag{5}$$

$$P_b(\lambda, T) = \frac{C_1}{\lambda^5 (e^{C_2/\lambda T} - 1)} \tag{6}$$

where $\rho(\lambda)$ is the sample spectral reflectance at a wavelength λ (measured by a standard UV–Vis-IR spectrophotometer) over the wavelength range of 300 nm to 2000 nm, C_1 is 3.743×10^{-16} Wm^2, C_2 is 1.4387×10^{-2} mK, and $P_b(\lambda, T)$ can be calculated by Plank's blackbody radiation Eq. (6), and T is 293 K [7,21]. Here, the use of emittance as the average absorption rate over 300 nm to 2000 nm aligns with the practical need to evaluate the coating's overall solar absorption efficiency and is used to provide a single representative value for the coating's ability to absorb solar energy in the relevant range.

2.3.4.4. FTIR spectroscopy. For materials which are infrared active, Fourier Transform Infrared Spectroscopy (FTIR) is typically used to identify the functional groups present in compounds by measuring their absorption of IR radiation over a range of wavelengths. Here, the FTIR in reflectance mode was conducted using a Nicolet™ iS™ 10 Spectrometer equipped with OMNIC software at ambient temperature, and the device was set for 32 scans within 4000 cm^{-1} to 400 cm^{-1}, which corresponds to IR wavelengths between 2.5 μm to 25 μm.

2.3.4.5. Infrared thermography. Infrared thermographic testing (for qualitative analysis) includes placing the samples onto an wooden plank
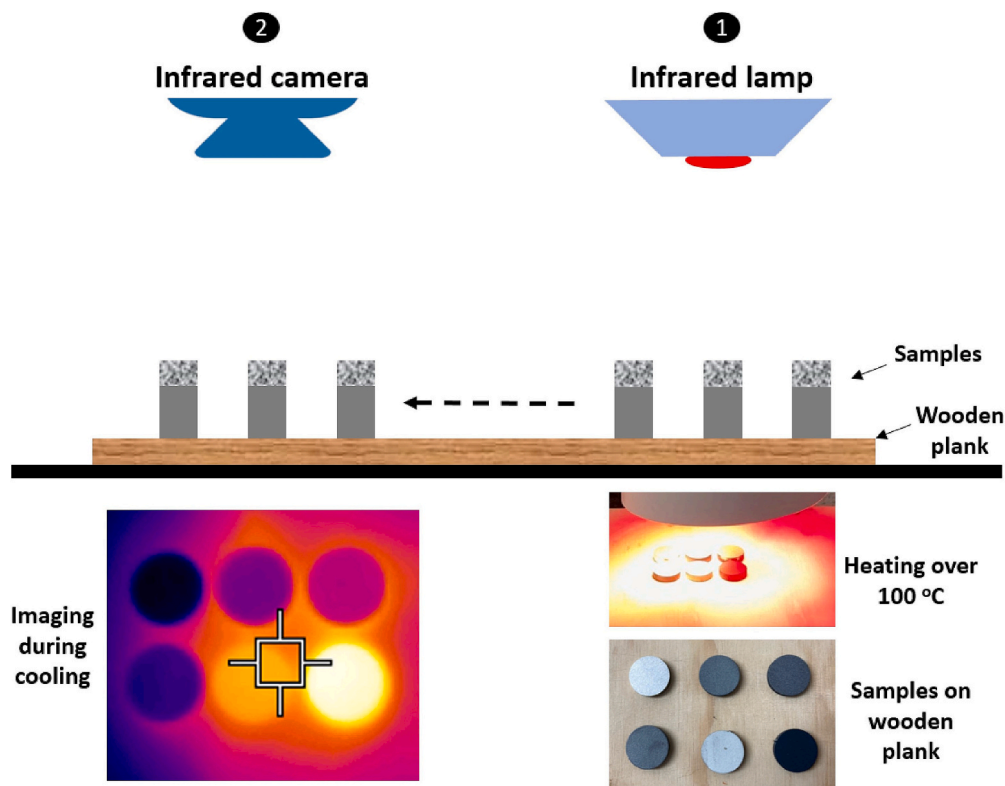
Fig. 2. Infrared (IR) thermography experiment (1: heating, 2: imaging).

(Fig. 2). In the first set of testing, the samples were heated by an infrared (IR) lamp (Beurer infrared lamp IL21, Infrared PAR 38, 150 W; infrared wavelength range: IR-A (760 nm to 1400 nm) and IR-B (1400 nm to 3000 nm), with dominant wavelength at 1100 nm) placed at a vertical distance of 60 mm, in the open air for 5 min and 10 min until the surface temperature of a sample exceeded 100 °C. The sample was then quickly moved under the IR thermal camera (FLIR TG167 which can measure temperature range: −25 °C to 380 °C, laser output: <1 mW and wavelength of 630 nm to 670 nm) for imaging.

In the second testing set, the samples were heated in a rapid chamber furnace (Carbolite, with maximum operating temperatures of 1200 °C) for 2 min at temperature setting of 235 °C and 280 °C (note: wave produced inside heating furnace could be in the IR range between 500 nm and 3000 nm). The samples were then quickly moved under the IR thermal camera for imaging. In the third set of testing, the samples heated for 2 min at 235 °C in a rapid chamber furnace and allowed to cool for 5 min in the open air, and then moved under the IR thermal camera for imaging. In all such testing, the samples did not show any observable degradation of coatings. A typical 0.95 emissivity value was set during the IR thermal camera imaging for all the samples tested. Part of the thermographic testing procedure for thermal spray coatings deployed here is adapted from Santangelo et al. (2017) [32].

2.3.5. Water absorbency test

There is general perception that in thermally sprayed ceramic coatings, water can easily be absorbed by the porous microstructure of the coating, and can influence the electrical insulation [33], and therefore the water absorbency tests were carried for samples under investigation. In First-Of-It-Kind investigation, water absorbency (qualitative) tests were performed using a 2 μl water drop under ambient condition to the surface of each samples, and observing the degree of droplet spread after 2 min. The samples were then heated under IR lamp for 5 min (until the surface temperature of a sample exceeded 100 °C), followed by observing dry patch to see the degree of water spread formed during

evaporation under heat and natural convection. The samples were swiftly placed under the IR thermal camera for imaging to observe the effects of limited infrared exposure. This analysis aimed to investigate the material's interaction with water molecules-whether through physical adsorption or chemical interaction-and their vibrational modes, which may absorb in specific infrared regions. Understanding this relationship is crucial for designing coatings optimised for specific IR behaviors, such as selective absorption or reflection. The analysis also included visual observation of the water drop (i.e., spreading, absorption, moisture redistribution and evaporation) and dry patch appearance onto the material after a set duration, and which material offers least absorbency [34].

3. Results and discussion

3.1. Microstructure

The surface morphology of the thermally sprayed coatings was examined using SEM, as depicted in Fig. 3. The observed microstructure of the coating revealed the presence of surface-connected, open-ended porosity, notably reaching up to 19 % in Mo-Mo2C/Al_2O_3 (thickness: 250 μm, single layer) and Mo-Mo2C/TiO_2 (thickness: 300 μm, single-layer), 16 % in Mo-Mo2C/ZrO_2 (thickness: 220 μm, single-layer), and approximately 10 % in NiO/YSZ (thickness: 250 μm, single-layer) and NiO/YSZ + 8YSZ (thickness: 300 μm, bi-layer), without the use of any sacrificial pore-forming materials. The porosity of the coated surface was analysed as the average of five area-normalised regions, each from image analysis Infinity Analyse software (Lumenera Corporation, R6.3) on the acquired SEM image. Thus, the porosity is not in 3D but a 2D measurement on the top surface. This software was used to measure porous area distribution for each coating surface (note: pore area ratio is defined as the sum of all pore areas divided by the total sample area analysed, and in this analysis, a thresholding (at 65 %) of the image individual pixel brightness as per the image analysis software was
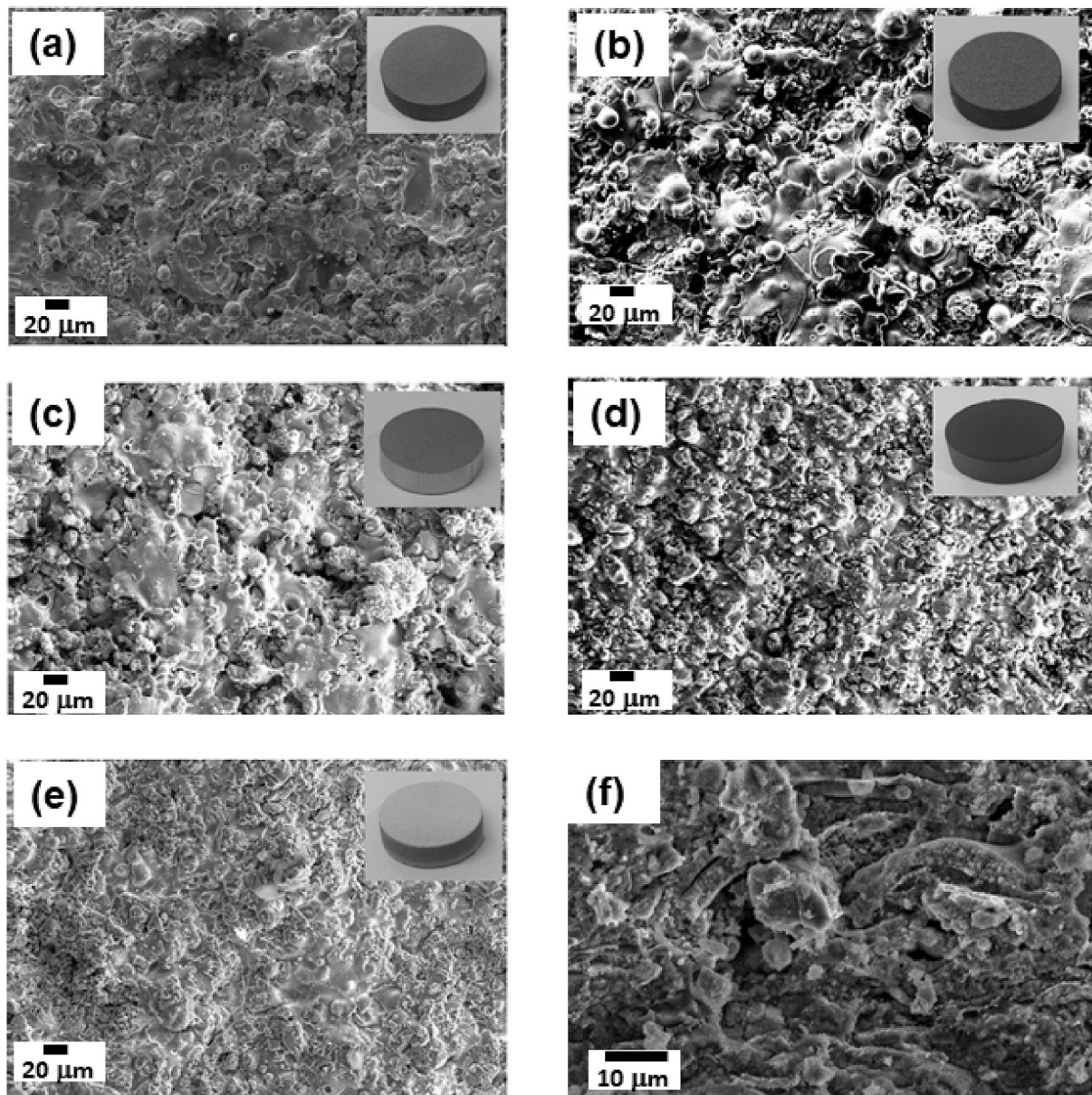
Fig. 3. Scanning electron microscopic (SEM) images of coating surface and coated disc (inset): (a) Mo-Mo$_2$C/Al$_2$O$_3$, (b) Mo-Mo$_2$C/TiO$_2$, (c) Mo-Mo$_2$C/ZrO$_2$, (d) NiO/YSZ, (e) NiO/YSZ + 8YSZ, and (f) fractured flake of NiO/YSZ (fractured flakes cross-section view).

manually set, so that the pore selection is not impaired or overestimated. In this way, it became possible to know the morphology of the pores. The proposed method to determine area percentage porosity is very similar to those proposed in ASTM E2109–01 (2021) [35]. Additionally, the microstructure exhibited voids, unmolten particles, non-bonded inter-splat regions and several other types of defects, including high roughness. Variations in splats and related features were noted, attributed to differing powder sizes and distinct process parameters.

Chemical elemental analysis (Fig. 4) was conducted to determine the distribution and weight percentage of elements in the coatings and Hastelloy®X substrate. As expected, the presence of various elements in the coatings was predominantly characterised by molybdenum (Mo) in the Mo$_2$C/Al$_2$O$_3$, Mo-Mo$_2$C/ZrO$_2$, and Mo-Mo$_2$C/TiO$_2$ coatings (Fig. 4 (a-c)). In Mo$_2$C/Al$_2$O$_3$, Mo-Mo$_2$C/ZrO$_2$, and Mo-Mo$_2$C/TiO$_2$ coatings, carbon (C) is part of the Mo$_2$C structure, meaning it may not be detected as free carbon. Since EDS primarily detects elements in their elemental or ionic forms, carbon incorporated into a stable compound is not identified separately. The NiO/YSZ coatings exhibited peaks

corresponding to elements such as Ni, Zr, O, C, Y, and Hf, while the NiO/YSZ + 8YSZ coatings showed peaks for elements including Zr, O, C, Y, and Hf (Fig. 4(d-e)). Traces of Hf in both NiO/YSZ and NiO/YSZ + 8YSZ coatings could be due to natural mix in zirconia raw materials [36]. Bare Hastelloy®X, a nickel-based superalloy, showing peaks corresponding to elements like Ni, Cr, Fe, Mo, Si, Al, and C [37].

The crystallographic phases of coated materials were analysed by X-ray diffraction (XRD), as shown in Fig. 5. The Hastelloy®X (mainly Ni, gamma phase) can be seen as a face-centred cubic (FCC) phase [12] (Fig. 5(a)). Since the coatings were thick, the substrate peaks were not visible in the coated specimens. The coating phases were body centred cubic (BCC) (molybdenum rich) in Mo-Mo$_2$C/Al$_2$O$_3$, Mo-Mo$_2$C/TiO$_2$, and Mo-Mo$_2$C/ZrO$_2$ (Fig. 5(b-d)). In Mo$_2$C/Al$_2$O$_3$, Mo-Mo$_2$C/ZrO$_2$, and Mo-Mo$_2$C/TiO$_2$ coatings with dominant Mo peaks, the presence of very small peaks for Mo$_2$C and other composition can arise from several factors, which are often related to the phase composition, crystallinity, and processing conditions of the coating. It could be due to high concentration of molybdenum (Mo), low crystallinity, as well as preferred
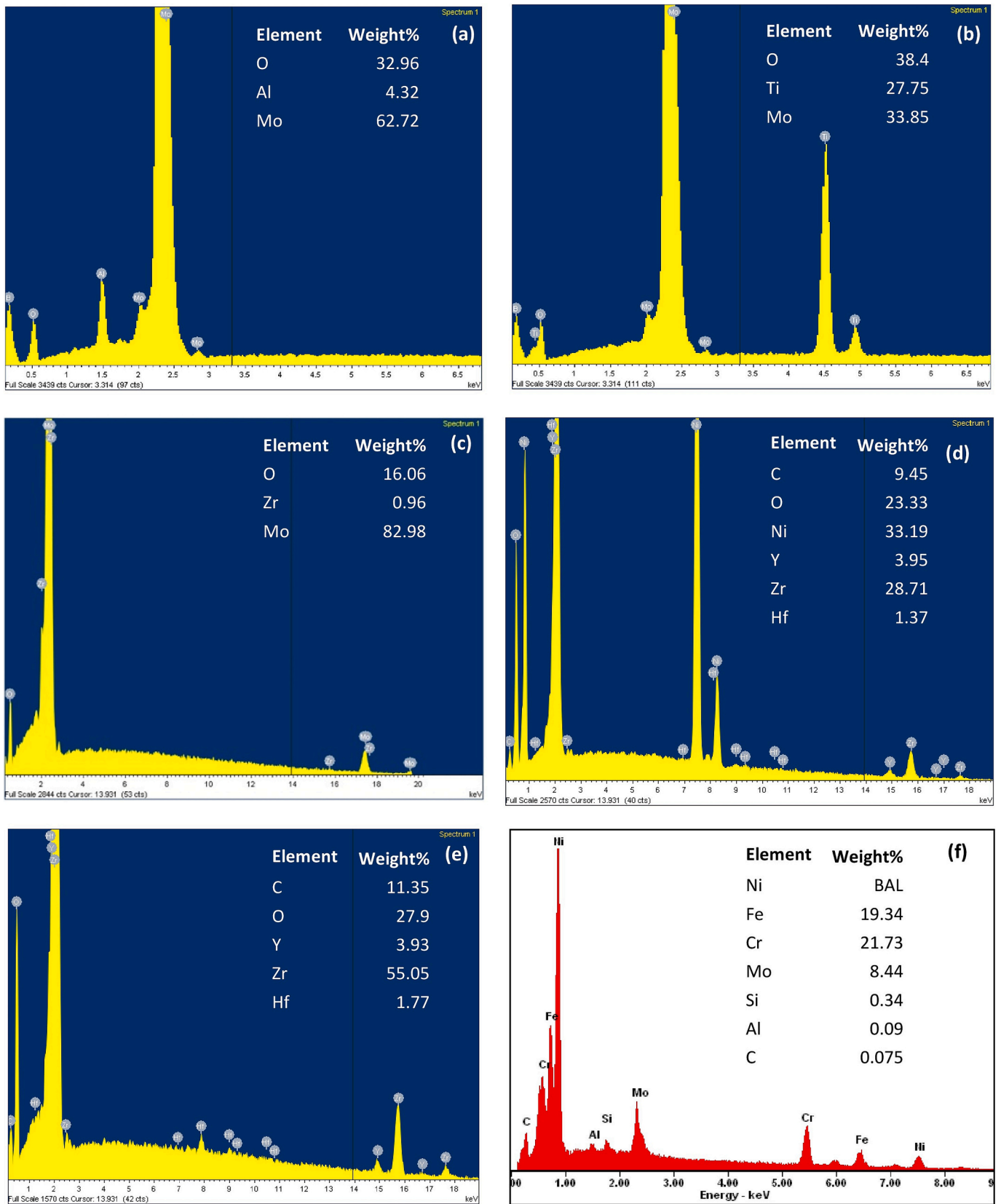
Fig. 4. Energy dispersive spectroscopy (EDS) of samples: (a) Mo-Mo$_2$C/Al$_2$O$_3$, (b) Mo-Mo$_2$C/TiO$_2$, (c) Mo-Mo$_2$C/ZrO$_2$, (d) NiO/YSZ, (e) NiO/YSZ + 8YSZ, and (f) bare Hastelloy®X.

Fig. 5. X-ray diffraction patterns of bare Hastelloy®X and coated samples (four intense reflections in coatings Mo-Mo$_2$C/ZrO$_2$, Mo-Mo$_2$C/TiO$_2$, and Mo-Mo$_2$C/Al$_2$O$_3$ corresponds to metallic Mo, in each pattern).

Fig. 6. Measured surface roughness of Hastelloy®X substrate and all coated samples.

texture leading to weaker diffraction signals. As for the NiO/YSZ, FCC phases of NiO and YSZ were identified, while a thin layer of 8YSZ coating on top of NiO/YSZ eliminated the NiO reflections (Fig. 5(e-f)).
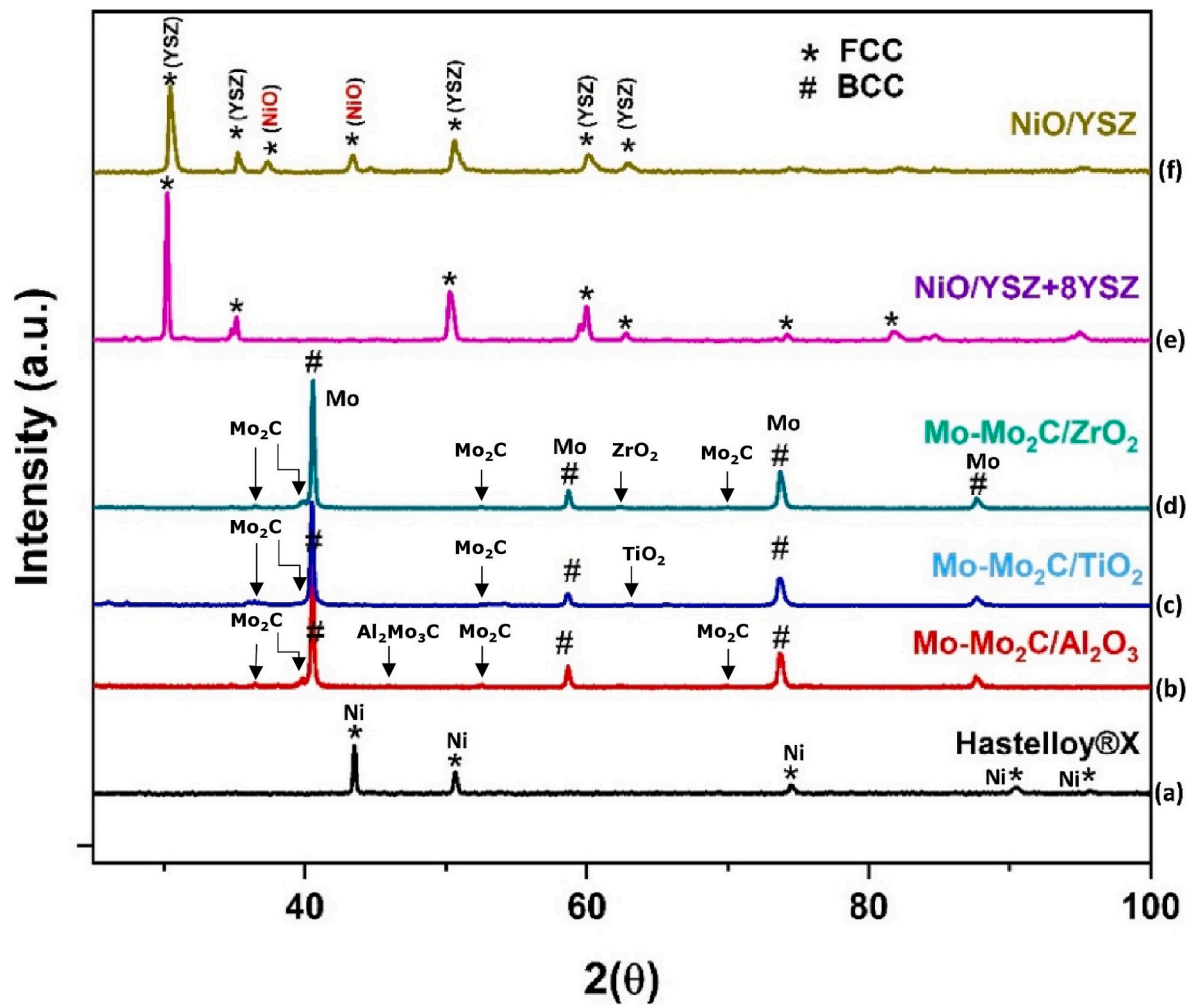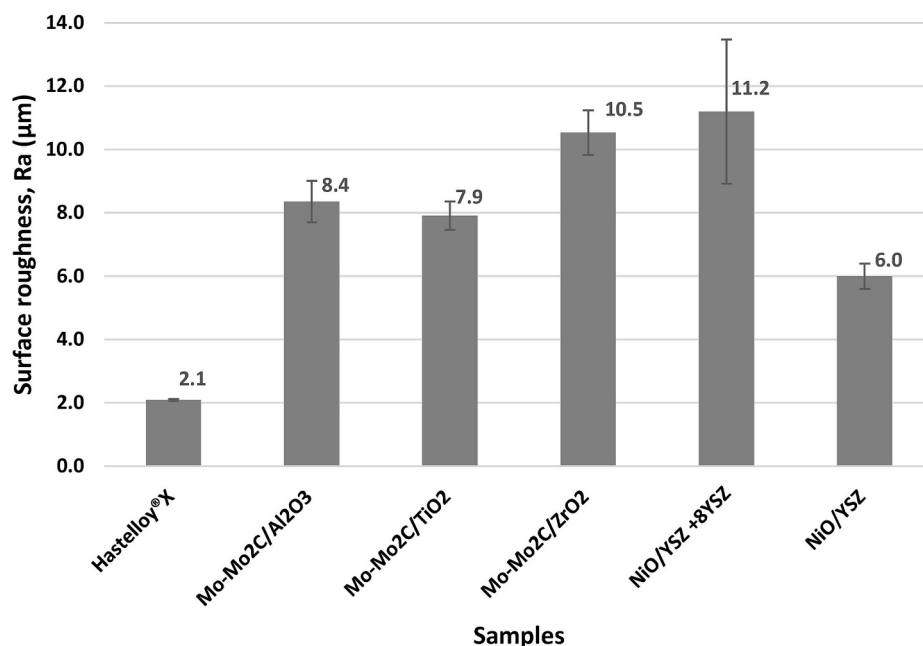
As shown in Fig. 6, the measured surface roughness (i.e., centre line average, R_a) are low for as-received Hastelloy®X substrate, but higher for all coated samples (with highest roughness for 8YSZ layer coated onto NiO/YSZ sample). The machine-cut as-received Hastelloy®X substrate surfaces exhibited low surface roughness, attributed to the precision of the machining process. In contrast, the coatings demonstrated significant variations in roughness, influenced by several factors related to the APS process, including material properties and spray parameters. Smaller powder particles are more likely to melt and flatten during deposition, while larger particles may remain semi-molten, resulting in increased surface roughness [38]. These factors impact how sprayed particles (molten or semi-molten) adhere to the substrate, their solidification behavior, and the resulting microstructure. Additionally, 8YSZ, a ceramic material commonly used in thermal barrier coatings, tends to exhibit higher roughness due to its brittleness, limited ductility, and characteristic splat morphology [39].

3.2. Sheet resistance

Sheet resistance (fifty measurements) were taken for each sample, and the average value was calculated. The average sheet resistance value for the Hastelloy®X substrate and when coated with Mo-Mo$_2$C/Al$_2$O$_3$, Mo-Mo$_2$C/TiO$_2$ and Mo-Mo$_2$C/ZrO$_2$ are given in Fig. 7. These coatings reduced the overall sheet resistance of the sample than the substrate. Mo-Mo$_2$C/TiO$_2$ coating exhibits the lowest resistance or higher conductivity vice versa.

Sheet resistance (which is a measure of lateral resistance per square area of coating with uniform thickness and an ability of electrical charge to travel in the plane of the coating layer). A lower sheet resistance in the coating layer leads to better electrical conductivity [40] (Fig. 7) and, consequently, less reflection of the incident light and better efficiency of the coated device. The low resistance of the coatings will ensure that charge carriers can move freely to the electrical contacts without many losses, further reducing reflection by facilitating effective carrier extraction. The samples coated with NiO/YSZ and NiO/YSZ + 8YSZ could not be measured as the sheet resistance of these two samples was larger than the equipment's limit at 10 MΩ/square, meaning these coatings exhibit extremely high resistivity.
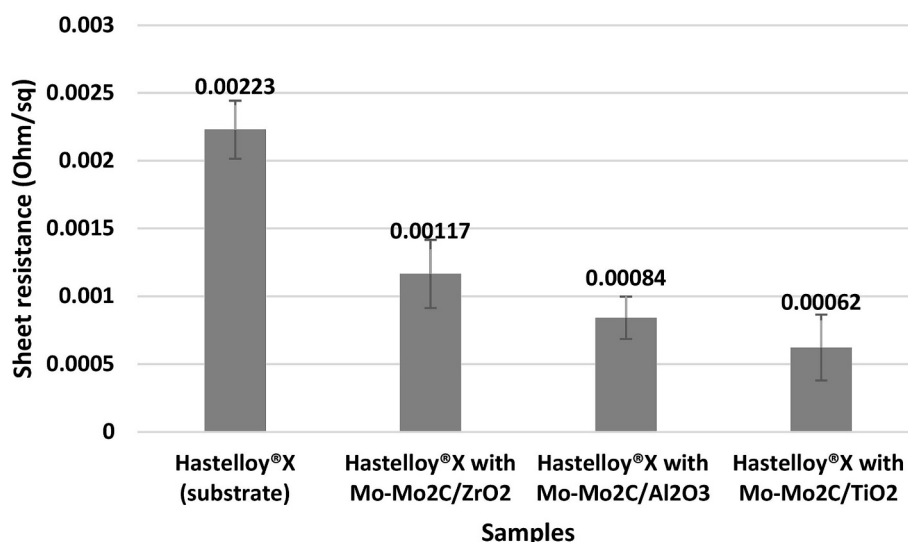
3.3. Relative permittivity

The capacitance measured for NiO/YSZ and NiO/YSZ + 8YSZ was used to calculate the relative permittivity of the coating using the technique described in *Section 2.3.3*. The other coatings (i.e., Mo-Mo$_2$C/Al$_2$O$_3$, Mo-Mo$_2$C/TiO$_2$, Mo-Mo$_2$C/ZrO$_2$) were observed to be conductive and hence their dielectric properties could not be measured. The measured capacitance (measured at 1 kHz) for NiO/YSZ and NiO/YSZ + 8YSZ were 0.142 nF and 0.105 nF, respectively. Thus, the relative permittivity of the two coatings was measured to be 15.55 and 9.58, respectively, with an error of about ±4 %. This error was calculated based on the 20 measurements performed for each coating. The relative permittivity of the materials directly impacts the electromagnetic wave (solar and near-IR light) propagation and their localisation within materials and contributed as the dielectric losses in the form of heat. In the graded layered system, it is beneficial to trap the radiation and reduce their emittance by providing another layer.

The measured relative permittivity values are comparable to those available in the literature. For example, for air plasma sprayed yttrium oxide (Y$_2$O$_3$) relative permittivity was between 10 and 13.5 [41], for YSZ ceramic relative permittivity was around 15.45 to 16.31 [42], and for YSZ coatings and sintered bulk YSZ, relative permittivity was around 15 to 32.5 for broad range of frequencies [43]. In the current work, compared to NiO/YSZ coating, the NiO/YSZ + 8YSZ coating showed lower bound relative permittivity, indicating minimal polarisation when subjected to an electric field, which corresponds to reduced ionic mobility but enhanced stability under high electric fields.

3.4. UV–vis-IR properties

Fig. 8 shows the solar reflectance of each sample (Hastelloy®X substrate and coatings). Fig. 8(a) shows the reflectance curves in UV–Vis-IR range wavelength for all coatings under different fabrication conditions (Table 1). In general, higher reflectance leads to lower absorption of light. However, NiO/YSZ + 8YSZ coatings have shown exceptional anti-reflective properties and the ability to absorb light across a wide range of wavelengths. This performance can be attributed to various factors, including the presence of absorptive materials, a porous surface structure that diffuses radiation instead of reflecting it, and the relative permittivity, which contributes to dielectric losses and traps light, ultimately contributing in the form of heat.

A higher reflectance was observed for NiO/YSZ coatings (around 0.4–0.5) compared to bi-layer NiO/YSZ + 8YSZ coatings (around 0.1)

Fig. 7. Sheet resistance of coated Hastelloy®X samples measured with the 4-point probe method (electrical) at ambient temperature.
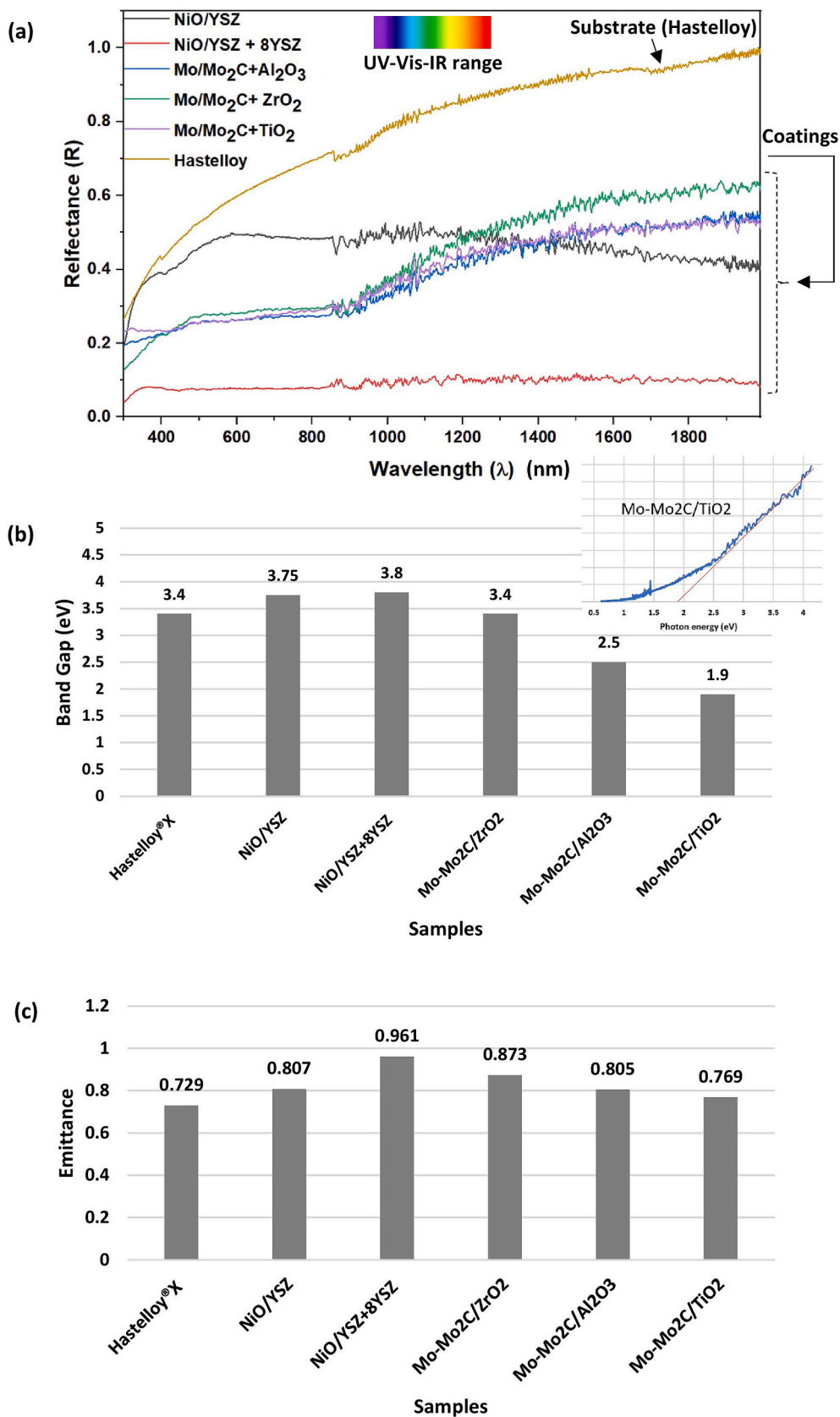
Fig. 8. Optical analysis at ambient temperature: (a) measured reflectance, (b) calculated indirect transition band gap (inbox: example Tauc plot shown for Mo-Mo$_2$C/TiO$_2$), and (c) calculated emittance.

(throughout the spectrum). Compared to other coatings (i.e., Mo-Mo$_2$C/Al$_2$O$_3$, Mo-Mo$_2$C/TiO$_2$, and Mo-Mo$_2$C/ZrO$_2$) in the UV–Vis region, a higher reflectance was observed for NiO/YSZ coatings. NiO/YSZ coatings showed a reflectance dip in the IR range, possibly due to a band gap transition. The reflectance of Mo-Mo$_2$C/Al$_2$O$_3$, Mo-Mo$_2$C/TiO$_2$, and Mo-Mo$_2$C/ZrO$_2$ coatings (around 0.2–0.6) was comparable throughout the spectrum. However, reflectance is more prominent in the IR region for the Mo-Mo$_2$C/ZrO$_2$ coatings. Though there is no data to have a direct comparison, but the measured reflectance can be compared to the reported Mo-rich DC sputtered thin film reflectance curve, which was as high as 0.57 within the near-infrared wavelength range from 400 nm to1200 nm [44]. Similarly, the higher reflectance results of Hastelloy®X (substrate only, which is a Ni-Cr-Fe-Mo alloy) can be compared with that of plain carbon steel (also called low carbon steel), which has been reported elsewhere [45].

The coating materials showed an energy transition corresponding to the energy of a photon in the wavelength range of solar electromagnetic wavelength (300 nm to 2500 nm, which corresponds to 4.1 eV to 0.5 eV energy). As per the methodology (Tauc plot) described in *Section 2.3.4*, Fig. 8(b) shows the calculated indirect transition band gap (3.8 eV to 1.9 eV, which approximately corresponds to 325 nm to 650 nm, i.e., visible band).

Fig. 8(c) shows the average emittance values (over 300 nm to 2000 nm) between 0.729 and 0.961, and the result shows that the 8YSZ top layer onto NiO/YSZ coating had high emittance (0.961), meaning that the material is effective at emitting thermal radiations compared to other materials. Though there is no data to have a direct comparison, but the reported emittance values for a range of 8YSZ coatings were broadly between ~0.3–1 (at λ = 2.5–22 µm) [46], ~0.3–0.95 (at λ = 3–13.5 µm) [47], and ~ 0.1–0.8 (at λ = 0.3–15 µm) [48], and the value varies significantly depending on the materials, microstructure, surface finish, temperature, and wavelength. The thick top layer of 8YSZ is expected to dominate the overall emittance, but may allow partial influence of the NiO/YSZ (underlying layer) on the system's effective emissivity. Rough and porous 8YSZ surface (including underlying NiO/YSZ layer) will also modify emissivity. For NiO/YSZ coating, the emittance value calculated was (0.807), and for a similar type of coating (i.e., Ni/YSZ), the reported emittance for range was ~0.7 [49]. The emittance values calculated for other coatings with dominant Mo metal were higher bound (such as Mo-Mo$_2$C/ZrO$_2$: 0.873, Mo-Mo$_2$C/Al$_2$O$_3$: 0.805) and Mo-Mo$_2$C/TiO$_2$: 0.769), and for Mo metals, the reported emittance for range were ~ Mo: 0.25–0.35 (unoxidized), 0.5–0.9 (oxidised) [50]. While the emittance of metal oxides varies significantly based on their composition, surface condition, and temperature, it is expected that the metal oxides (ZrO$_2$, Al$_2$O$_3$ and TiO$_2$) and metal-metal carbide (Mo-Mo$_2$C), with their robust stability in thermal environments, offering a transcendent balance of low and high emittance regions. Similarly, emittance of Hastelloy®X is scarce data, but some literature reported values of around ~0.84 [51] and ~0.18–0.28 [52]. In the current analysis, the Hastelloy®X (substrate only, machine-cut non-polished surface) showed high emittance of 0.729, meaning the metal is effective at emitting thermal radiation compared to the coating materials, especially in high temperature applications [53].

The reflectance of waves are also directly influenced by surface roughness and also play a role to trap solar energy [54]. Therefore, comparisons have been made between the surface roughness and the substrate, as shown in Fig. 6, the measured surface roughness (i.e., centre line average, R_a) are low for Hastelloy®X substrate, but higher for all coated samples. The NiO/YSZ + 8YSZ coating exhibits higher roughness and lower porosity (~10 %) when compared to other coatings.

The relationship between solar reflectance and thermal emittance is governed by a material's interaction with incident radiation and its thermal properties [55,56]. Solar reflectance primarily pertains to visible and near-IR wavelength range, while thermal emittance is related to IR wavelength range [57]. Reflectance is measured relative to

incident energy (such as sunlight), whereas emittance is typically based on a material's thermal energy. Both solar reflectance and thermal emittance can vary depending on the direction of the incident or emitted radiation and aggregating these values does not necessarily equal 1 because they describe two different physical properties related to a material's interaction with sunlight and heat [58,59].

3.5. Infrared properties

FTIR typically exhibit characteristic absorption bands in the spectrum corresponding to the vibrational modes of the atoms and bonds within the compound (note: complex mix of inorganic compound in the present work, Fig. 9), which include bond stretching and bending vibrations, as well as functional groups vibration present in the compound [60]. For example, metal-oxygen bonds in a metal oxide could typically give rise to strong absorption bands in the infrared region. Meanwhile, infrared radiation focuses on the emission of infrared radiation by materials when heated. The heating could be under various sources, e.g., IR lamp heating or furnace heating or others. While both (i.e., FTIR and infrared radiation) involve the interaction of materials with infrared radiation, they serve different purposes and can be used in different contexts.

3.5.1. FTIR absorption analysis

Fig. 9(a) is FTIR spectra of neat Hastelloy®X substrate, whereas Fig. 9(b) to (f) show the remaining five samples coated with various layers such as Mo-Mo$_2$C/Al$_2$O$_3$, Mo-Mo$_2$C/TiO$_2$, Mo-Mo$_2$C/ZrO$_2$, NiO/YSZ + 8YSZ, and NiO/YSZ, respectively, (Hastelloy®X showed sharp peaks at 2375 cm^{-1}, 2346 cm^{-1}, 2158 cm^{-1}, 2031 cm^{-1}, and 1978 cm^{-1}), which were also noticeable for the rest of the samples. A closer look at the wavenumber range of 500 cm^{-1} to 1000 cm^{-1} is shown in the inset. All these wavenumbers in the Hastelloy®X sample correspond to surface contaminants, such as atmospheric moisture, contributing to regional absorption or the formation of surface oxide layers. A common noticeable peak can be seen at 2917 cm^{-1} in NiO/YSZ and Mo-Mo$_2$C/Al$_2$O$_3$, whereas NiO/YSZ + 8YSZ and Mo-Mo$_2$C/TiO$_2$ showed broader features (bending vibrations). However, there was no sign of a peak for Hastelloy®X and Mo-Mo$_2$C/ZrO$_2$ at 2917 cm^{-1}. The peak at 2917 cm^{-1} was noticeable in four out of six samples, as both narrow and broad peaks are likely due to post-fabrication carbonaceous surface contaminants where these samples could come in contact with, reflecting on the surface. This peak was not produced during fabrication, as all six samples were processed at high temperatures. Also, a substantial shoulder peak was observed in NiO/YSZ and Mo-Mo$_2$C/TiO$_2$ at 2960 cm^{-1}, which could be due to organic contaminants on the surface due to handling or processing. A broad absorption peak was seen around 3400 cm^{-1}, which corresponds to the adsorbed water on the surface and its stretching vibration in almost all the samples (i.e., oscillations of chemical bonds along the bond axis which leads to bond length change).

The peaks close to 400 cm^{-1} seen in Fig. 9(e) and (f) are characteristic of metal-oxygen-metal vibrations i.e., Ni-O-Ni, Y-O-Y and Zr-O-Zr [61]. The peak near 410 cm^{-1} is attributed to Ni-O-Ni vibration, whereas the peak at 415 cm^{-1} is attributed to the Y-O-Y bond vibration. Moreover, the broad absorption peak, which is seen from 400 cm^{-1} to around 600 cm^{-1} in Fig. 9(e), is due to the Ni—O stretching vibration. From Fig. 9(c), the wide band observed at around 1380 cm^{-1} is attributed to the Ti—O vibrational modes [62,63].

Additionally, for Mo-Mo$_2$C/TiO$_2$ with titanium oxide coating, stretching bands at an approximation of 710 cm^{-1} and 870 cm^{-1} are noticeable due to Ti—O stretching vibration (Fig. 9, inset), which was assigned at 690.52 cm^{-1} from previous work [64]. For the zirconium oxide coating (Fig. 9(d)), a weak peak at 670 cm^{-1} and 870 cm^{-1} represents Zr—O vibration [65]. A similar trend of peaks, which was prominent for Mo-Mo$_2$C/ZrO$_2$, can also be seen for NiO/YSZ + 8YSZ (Fig. 9(e) and (f)). Other peaks at 875 cm^{-1} and 713 cm^{-1} were also noticeable for NiO/YSZ and NiO/YSZ + 8YSZ (Fig. 9(e) and (f)),
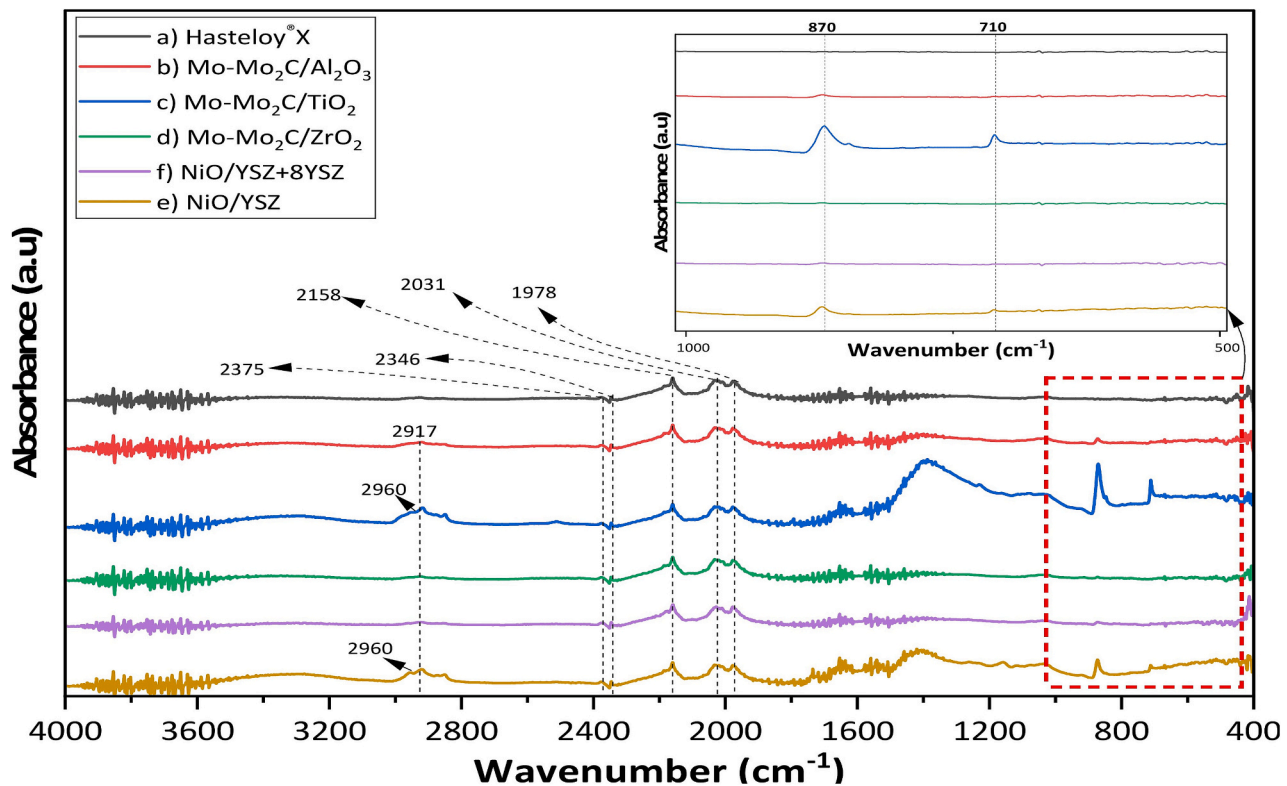
Fig. 9. FTIR absorbance measurements (between 400 cm^{-1} to 4000 cm^{-1} wavenumber, which corresponds to infrared wavelengths between 25 μm to 2.5 μm): (a) Hastelloy®X (substrate only), (b) Mo-Mo$_2$C/Al$_2$O$_3$, (c) Mo-Mo$_2$C/TiO$_2$, (d) Mo-Mo$_2$C/ZrO$_2$, (e) NiO/YSZ + 8YSZ, and (f) NiO/YSZ coatings.

indicating the presence of Ni—O stretching vibration.

FTIR spectra observed for a material depend heavily on the processing method used. Thermal spray, being a high-temperature process characterised by rapid cooling, induces a combination of compressive and tensile residual stresses in the coating [13]. Residual stresses alter the bond lengths and bond angles in the material, which changes the vibrational energy levels of molecular bonds, usually resulting in the increase and decrease of a characteristic wavenumber, respectively [66]. As FTIR spectroscopy provides the composition of materials by measuring the absorption of infrared radiation, which can enable qualitative and quantitative investigation of materials, further insights are still needed in the adsorption of molecules for complex classes of materials [60].

3.5.2. Infrared radiation (qualitative) analysis

Samples whose temperature exceeds absolute zero (−273.15 °C or 0 K) emit infrared (IR) radiation. The IR radiation consists of the emission, transmission and reflection of IR emitted by samples within the visual field of the thermal camera. An IR thermal camera measures the infrared radiation (long wavelength) emitted by the samples, and it translates the IR spectrum wavelengths into wavelengths detectable to the human eye (colours). It is important to note that the intensity of the IR radiation emitted by the sample depends on the materials surface, i.e., shiny, smooth, or reflective surface typically have a slightly lower emissivity than structured surfaces of the same material. For example, a mirror finished metal surface have low emissivity than a rough surface. Therefore, all coated and bare substrate emissivity colour map were recorded to qualitatively analyse the emittance properties of the coating, as shown in Fig. 10. The interpretation of these results was repeatable in all scenarios. The NiO/YSZ sample followed by the NiO/YSZ + 8YSZ were the brightest, whereas Hastelloy®X was the darkest with others being intermittent. The brightest colour associated with the NiO/YSZ sample suggested that the IR emission was high, whereas Hastelloy®X was dark, which means the IR emission was lower due to machine-cut

non-polished surface.

The relative difference in the brightness of the NiO/YSZ coating compared to the bi-layer coating (8YSZ deposited on NiO/YSZ) under IR lamp or furnace heating (Fig. 10) can be attributed to several key factors related to emissivity, reflectance, and thermal radiation properties of the materials in the two coatings. NiO is known for high absorption and has high emissivity in the IR region (>0.5) [67], meaning it absorbs and emits thermal radiation efficiently. YSZ (which contributes additional emissivity with values ~0.46–0.56 [68]) is generally transparent to Vis- and IR light but strongly absorbs in the UV-range (note: the reported emittance for Ni/YSZ was ~0.7 [49]). 8YSZ is typically transparent or weakly absorbing in much of the Vis- and IR-region [69–71] (note: as discussed in section above, the reported emittance for 8YSZ were very broad, i.e., ~0.3–1 [46], ~0.3–0.95 [47], and ~0.1–0.8 [48]). The 8YSZ deposited on NiO/YSZ acts as an additional thermal barrier layer and may have slower or reduced thermal radiation emission compared to the NiO/YSZ coating. The observation highlights an interplay between the material properties, microstructure, and optical behavior of 8YSZ and NiO/YSZ. The combination of emissivity, reflectance, and thermal radiation properties modifies the system's thermal radiation properties, and the intention is to balance optical and thermal emission for optimal performance in demanding environments.

The optimisation of the coating powder materials and particle sizes, along with the coating process parameters, can be used to deposit coatings with tailored surface roughness and pore structures. As shown in the SEM images and roughness measurement shown earlier point to the surfaces with high roughness (Fig. 6) will have higher surface areas (e.g., NiO/YSZ + 8YSZ) compared to smoother surface (e.g., Hastelloy®X), and higher surface area provides more sites for thermal radiation to be emitted from, leading to increased thermal emittance. When the incident electromagnetic wave interacts with the rough surface, due to multiple reflections and interactions, it gets trapped within surface morphology or gets absorbed by the material. Higher absorption due to surface morphology leads to increased thermal emittance as more
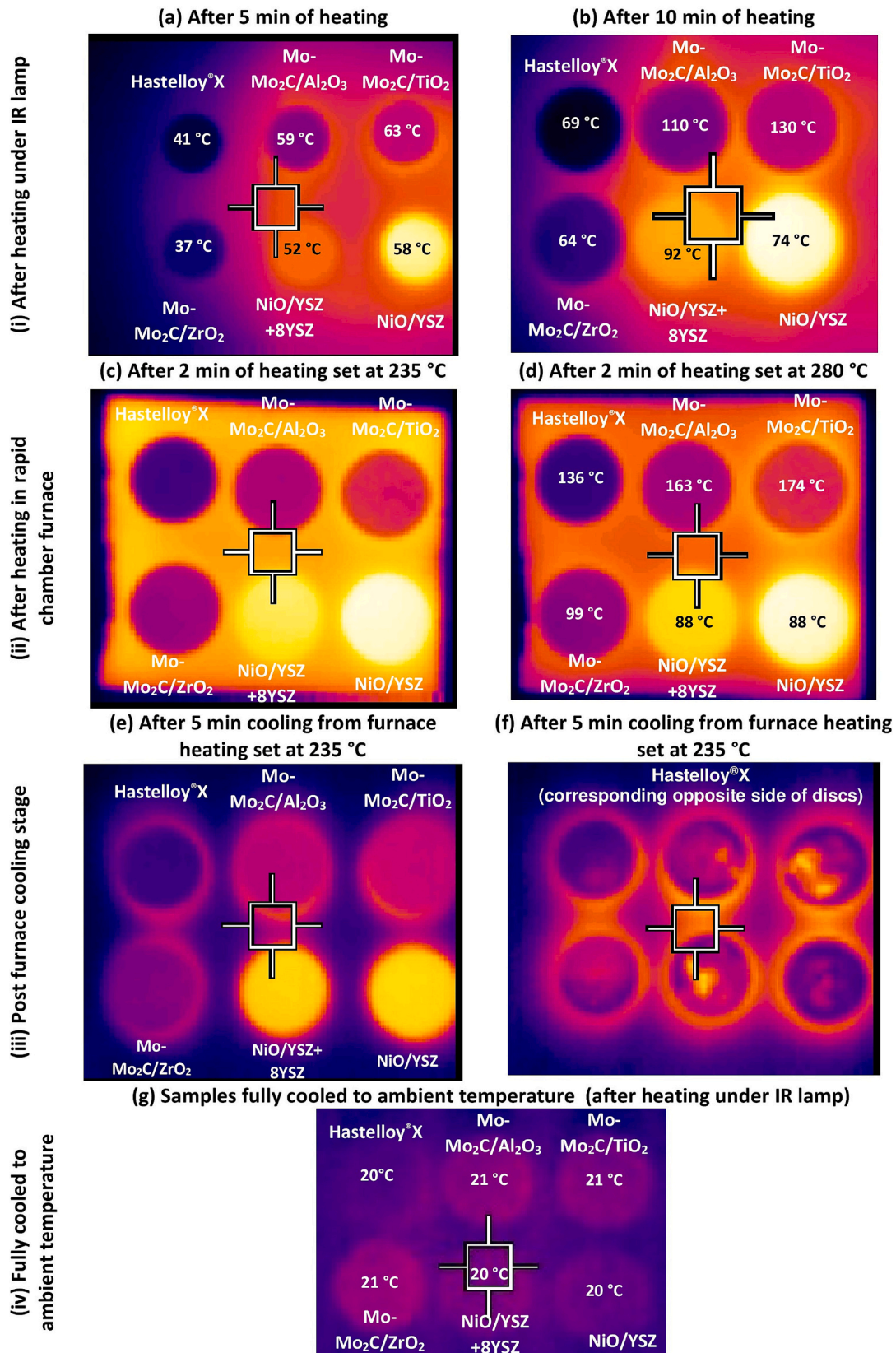
Fig. 10. Infrared emissivity colour map of samples in the open air: (i) soon after heating under IR lamp (surface temperature shown measured soon after 5 min and 10 min of heating under IR lamp), (ii) soon after heating in furnace (surface temperature shown measured soon after 2 min of furnace heating at 280 °C), (iii) post furnace cooling stage: after 5 min of heating, and (iv) samples fully cooled to ambient temperature (after heating in furnace).

absorbed energy is re-emitted as thermal radiation [72,73].

Material composition and their properties (e.g., conductivity, emissivity, and absorption coefficient) are also critical in determining thermal emittance. These materials have the potential to be explored in heating applications where the coating not only protects the overheating heating of the substrate, e.g., Fig. 10(ii)(d), where the coating is at a lower temperature of 88 °C vs the substrate temperature of 136 °C, but also improving the efficiency of the heating process using the infrared spectrum as indicated by the brightness of the coating. Other radiation and insulation properties applications could include thermionic applications and sensors [74]. Further research is, however, required to explore potential materials which need to be tailored to specific applications requiring infrared emissions.

3.6. Initial water droplet absorption analysis and effect of infrared heating

In the current analysis, as shown in Fig. 11, the idea of initial water droplet absorption (qualitative) analysis is to assess the coating

materials absorbency. Initial water droplet absorption test measures the degree of absorbency of the porous material due to initial capillary action. Droplet absorption and spreading on the surface are known to be dependent on multiple properties of liquid and materials (e.g., viscosity, density, surface tension, liquid drop conditions, pore size and distribution, hydrophobicity, and surface wettability and roughness) [34]. As shown in Fig. 11(a, b), the experiments were performed using a 2 μl water drop (can be classed as a very small and thinner drop) under ambient condition to the surface of each samples, Fig. 11(c) shows the degree of spread in a droplet after 2 min, Fig. 11(d) shows the samples with water drops being exposed to IR radiation and heated, and corresponding infrared image (after 1 min of heating under IR lamp, Fig. 11 (e)), and (f) shows dry patch indicating the degree of water absorption during evaporation under heat and natural convection for 5 min.

As can be seen in Fig. 11(a,b), water droplet is relatively transparent on all sample surface in the visible (Vis-) spectrum, but shows 'cold' or 'opaque' areas (Fig. 11(e)) because the IR radiation does not pass through them effectively, as water strongly absorbs IR radiation due to its molecular vibrations [75]. Other observation shows (Fig. 11(c)) that

(a) Single water droplet is being applied

(b) Water droplet applied on the surface (<30 sec)

(c) Degree of droplet spread after 2 minutes

(d) Exposure to infrared radiation

Water evaporation and absorption in progress during heating (heated for 5 minutes, until water droplets evaporated/absorbed leading to dry patch)

(e) IR imaging after 1 min of infrared exposure

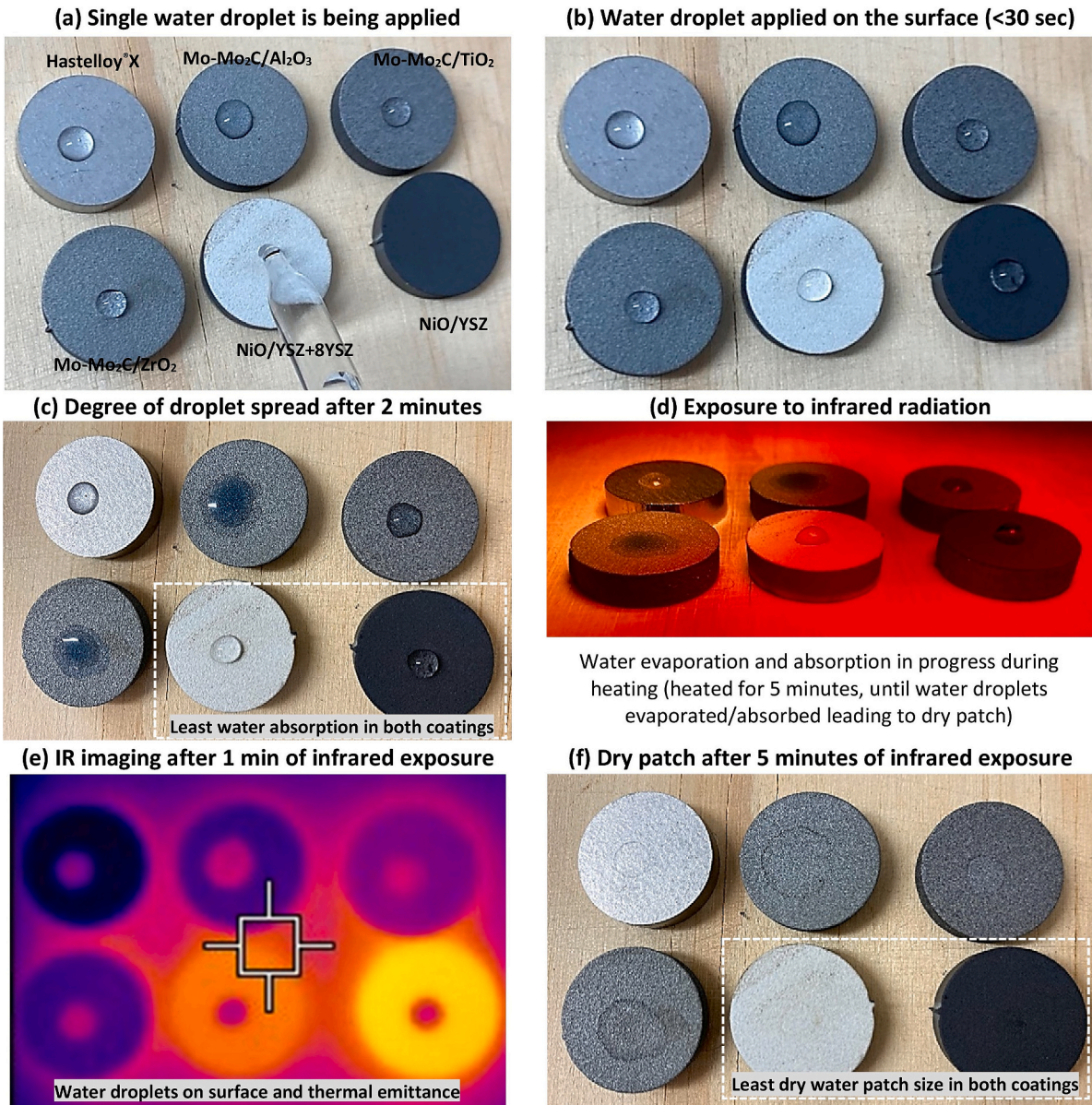**(f) Dry patch after 5 minutes of infrared exposure**

Fig. 11. Initial water droplet absorption test and the effect of limited infrared (IR) exposure.

the two coatings (i.e., NiO/YSZ + 8YSZ and NiO/YSZ, both not inherently hydrophobic [76]) offers insufficient or least absorbency by the microstructure due to small pore size and low surface-connected porosity (~10 %), and Hastelloy®X showed insufficient absorbency but due to solid (non-porous) surface microstructure, within the given test duration. With time, the water mass absorbed in other coatings (i.e., Mo-Mo$_2$C/Al$_2$O$_3$, Mo-Mo$_2$C/ZrO$_2$, Mo-Mo$_2$C/TiO$_2$) increases, possibly due to high pore size and surface connected porosity (~16 % to 19 %), including some potential effect of hydrophilic behavior of metal oxides [77] and molybdenum carbides [78]. Due to the presence of entrapped air in the porous material, the absorption can be hindered, and afterwards, a capillary contact could occur and absorption could go on until depletion, concurrently with evaporation at the surface [34].

Overall observation shows that water droplets after being exposed (heated) to infrared for a short duration (Fig. 11(d)) gets warmer and emits thermal radiation and impacting heat transfer efficiency. Wet areas will tend to retain heat longer or exhibit evaporative cooling, appearing cooler in IR image, whereas dry areas will heat up or cool down faster, creating a thermal contrast visible in the IR spectrum (Fig. 11(e)). The thermal emittance of the water droplets is expected to increase with the increase in its temperature, but water will also get evaporated, absorbed, and leaving the dry patch (Fig. 11(f)). Occurrence of dry water patch after heating could be driven by the energy transfer from the heat source to the water molecules, as well as action of specific forces (gravity, surface tension, or shear force caused by the surrounding airflow) [79], leading to droplet conversion from the liquid phase to the vapor phase.

Considering the environmental impact on the application of such coatings for reduced reflectance, due to varied degree of porous structure of coatings, absorbed moisture (water droplets) will enter the coatings differently and will fill the pores along the surface connected porosities. Consequently, the optical reflectance (in UV–Vis-IR range) of the coatings will get modified in accordance with temperature, and requires further investigation. Water has a different thermal conductivity compared to the material and ambient air. When pores are filled with water, the effective temperature, thermal conductivity, absorptivity, emissivity, and refractive index of the top surface of the porous layer

may change, which could influence heat transfer within the material, leading to changes in the overall thermal emittance. Such study (experimental, analytical and numerical) needs to consider dynamics of the droplet as well as the optical characteristics of porous medium. Overall, the fate of droplets being absorbed into the porous media is still far from being understood [80–83], and spreading (including hydrophobicity) of water droplets on porous thermally sprayed coatings could be the subject of further studies [84].

3.7. Opportunities

The coating materials and characteristics play an important role in optical and thermal radiation properties. For thermally sprayed coatings, microstructural defects, high surface roughness and phase content variations can lead to poor functional properties, which limits the fabrication of solar selective absorbers. However, as demonstrated through this research, thermal spray offers the flexibility of manufacturing coating designs and phases to improve optical and thermal radiation properties.

Multi-material composite coatings can absorb electromagnetic wave in a wide wavelength range. When a material is irradiated with incident photons of a certain wavelength or range of wavelengths, the energy of the incident photons will excite the atoms from the ground state to the higher state or can cause the molecules of the material to vibrate, so that the incident light can be absorbed selectively. There are many potential advantages of employing multi-material composite coatings (single-layer or bi-layer, see Fig. 12) for absorption in the UV–Vis-IR range. For example, the material could be tailored such that the absorption matches a specific wavelength to enhance the absorption efficiency, introduce tuning and filtering effects, or improve sensing characteristics. Alternatively, metamaterials design can be created with alternative materials array to get tailored band gaps in an arrayed structure [8].

This work highlights the importance and opportunity to develop large area coating of wide band (UV–Vis-IR region) anti-reflecting surfaces by employing versatile APS technique. In addition to understanding the structural properties of coatings (e.g., NiO/YSZ and NiO/YSZ + 8YSZ), the optical and optoelectronic properties (low relative
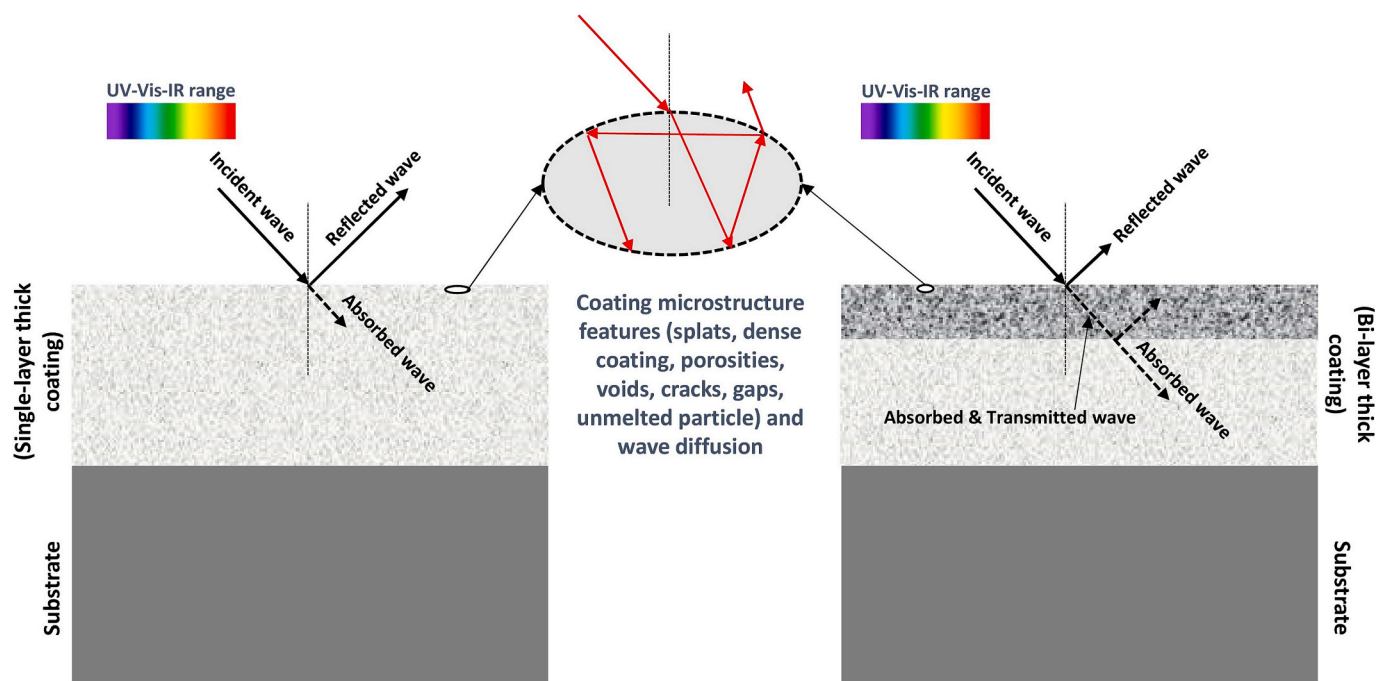

Fig. 12. Schematic of simplifed electromagnetic wave (UV–Vis-IR) interaction with the coating (single-layer, bilayer, and representative microstructural features in coating).

permittivity, low optical reflectance, high translucency or transparency, and tunable bandgaps) are expected to hold great promise in applications such as solar absorber coating, photovoltaics, optical sensors, stealth and optical communication systems. Moreover, this multi-material proof-of-concept study is an important step in exploring the capability of coatings for a wide range of optoelectronic applications such as thermionic (hot) electrodes, a thermionic emissive layer, light-induced local heaters, or optically activated thermal switches for integrated photonics [85,86].

4. Conclusions

Addressing the limitations in solar thermal energy conversion efficiency, this study propose a new pathway to fabricate bi-layer (duplex) composite coatings using air plasma spray to enhance light absorption and thermal emission properties. Five different composite coatings were deposited on Hastelloy®X substrates namely, single-layer $Mo-Mo_2C$/ceramic (i.e., Al_2O_3, ZrO_2, TiO_2) and NiO/YSZ, and a bi-layer NiO/YSZ with an additional 8YSZ top layer. Characterisation focused on the ultraviolet-visible-infrared (UV–Vis-IR) spectral range to assess light-matter interactions. Key findings were:

a. The surface roughness of all coated as-sprayed samples was higher, with the highest roughness observed for the 8YSZ layer on NiO/YSZ, influenced by factors such as material choice and spray parameters during the APS process.
b. All coatings achieved minimal light reflectance (0.1–0.6), indicating effective solar energy capture. Notably, the bi-layer NiO/YSZ + 8YSZ system exhibited exceptionally low reflectance ($\sim$0.1), highlighting its superior potential for solar energy absorption.
c. The $Mo-Mo_2C$/ZrO_2 coating revealed a distinct characteristic with higher reflectance specifically in the infrared region. This warrants further investigation to understand potential benefits or drawbacks for solar thermal applications with tailored spectral selectivity.
d. A strong correlation was observed between light absorption and thermal emission properties. The highly absorbing NiO/YSZ + 8YSZ coating achieved a superior thermal emittance ($\sim$0.961), signifying efficient heat re-emission at desired operating temperatures.
e. While the NiO/YSZ coating performed well with moderate reflectance ($\sim$0.5) and emittance ($\sim$0.8), it was surpassed by the bi-layer system. Additionally, the NiO/YSZ + 8YSZ system exhibited lower relative permittivity compared to NiO/YSZ, indicating its potential as a better insulator. The low optical reflectance and transparent properties of the 8YSZ top layer further contribute to the bi-layer system's outstanding overall performance.
f. Over the test duration, NiO/YSZ + 8YSZ and NiO/YSZ coatings exhibited the least water absorbency due to small pore size and low surface-connected porosity ($\sim$10 %). In contrast, coatings like $Mo-Mo_2C$/Al_2O_3, $Mo-Mo_2C$/ZrO_2, and $Mo-Mo_2C$/TiO_2 showed increasing water absorption, likely due to larger pore sizes and higher surface-connected porosity ($\sim$16 %–19 %). Observations showed that water droplets exposed to infrared heat became warmer and emitted thermal radiation, influencing heat transfer efficiency.

Our suggested findings underscore the potential of thermal spray coatings technology to develop advanced selective surfaces for solar thermal systems. Future efforts should focus on optimizing bi-layer (duplex) coating composition, microstructure, and thickness to further enhance light absorption and thermal emission.

CRediT authorship contribution statement

Nadimul Haque Faisal: Writing – original draft, Visualization, Validation, Supervision, Software, Resources, Project administration, Methodology, Investigation, Funding acquisition, Formal analysis, Data curation, Conceptualization. **Vinooth Rajendran:** Writing – review &

editing, Resources. **Siva Kaniapan:** Writing – review & editing, Resources, Investigation, Formal analysis. **Vinoth Ramalingam:** Writing – review & editing. **Anil Prathuru:** Writing – review & editing, Formal analysis. **Rehan Ahmed:** Writing – review & editing, Investigation, Funding acquisition. **Nirmal Kumar Katiyar:** Writing – review & editing, Visualization, Validation, Formal analysis. **Aakash Bansal:** Writing – review & editing, Resources, Methodology. **Thomas Whittaker:** Writing – review & editing, Resources, Methodology, Formal analysis. **Patrick Isherwood:** Writing – review & editing, Resources, Methodology, Formal analysis. **Will Whittow:** Writing – review & editing, Resources, Methodology, Funding acquisition, Formal analysis. **Mohamed Egiza:** Writing – review & editing. **Saurav Goel:** Writing – review & editing, Resources, Funding acquisition.

Declaration of Generative AI and AI-assisted technologies in the writing process

During the preparation of this work, the author(s) used AI assistance to improve the readability and language of the manuscript. The authors reviewed and edited the final content and took full responsibility for the content of the published article.

Declaration of competing interest

The authors declare that they have no known competing financial interests or personal relationships that could have appeared to influence the work reported in this paper.

Acknowledgements

Data availability

Data will be made available on request.

References

[1] L. Noč, I. Jerman, Review of the spectrally selective (CSP) absorber coatings, suitable for use in SHIP, Sol. Energy Mater. Sol. Cells 238 (2022) 111625, https://doi.org/10.1016/j.solmat.2022.111625.
[2] X. Yan, M. Shatalov, T. Saxena, M.S. Shur, Deep-ultraviolet tailored- and low-refractive index antireflection coatings for light-extraction enhancement of light emitting diodes, J. Appl. Phys. 113 (2013) 163105, https://doi.org/10.1063/1.4802663.
[3] D.B. Mahadik, R.V. Lakshmi, H.C. Barshilia, High performance single layer nano-porous antireflection coatings on glass by sol–gel process for solar energy applications, Sol. Energy Mater. Sol. Cells 140 (2015) 61–68, https://doi.org/10.1016/j.solmat.2015.03.023.
[4] R. Yusoh, M. Horprathum, P. Eiamchai, P. Chindaudom, K. Aiempanakit, Determination of optical and physical properties of ZrO_2 films by spectroscopic ellipsometry, Procedia Eng. 32 (2012) 745–751, https://doi.org/10.1016/j.proeng.2012.02.007.
[5] K.O. Ukoba, A. Eloka-Eboka, F.L. Cinambao, Review of nanostructured NiO thin film deposition using the spray pyrolysis technique, Renew. Sust. Energ. Rev. 82 (2018) 2900–2915, https://doi.org/10.1016/j.rser.2017.10.041.
[6] P. Chen, X. Li, F. Tian, Z. Liu, D. Hu, T. Xie, Q. Liu, J. Li, Fabrication, microstructure, and properties of 8 Mol% yttria-stabilised zirconia (8YSZ) transparent ceramics, J. Adv. Ceram. 11 (2022) 1153–1162, https://doi.org/10.1007/s40145-022-0602-6.

N.H. Faisal et al.

Surface & Coatings Technology 498 (2025) 131854

[7] K. Xu, M. Du, L. Hao, J. Mi, Q. Yu, S. Li, A review of high-temperature selective absorbing coatings for solar thermal applications, J. Mater. 6 (2020) 167–182, https://doi.org/10.1016/j.jmat.2019.12.012.

[8] N.H. Faisal, N. Sellami, F. Venturi, T. Hussain, T. Mallick, F. Muhammad-Sukki, A. Bishop, H. Upadhyaya, N.K. Katiyar, S. Goel, Large scale manufacturing route to metamaterial coatings using thermal spray techniques and their response to solar radiation, Emerg. Mater. 4 (2021) 1619–1633, https://doi.org/10.1007/s42247-021-00252-z.

[9] N.H. Faisal, R. Ahmed, N. Sellami, A. Prathuru, J. Njuguna, F. Venturi, T. Hussain, H.Y. Nezhad, N.K. Katiyar, S. Goel, H. Upadhyaya, S. Joshi, F. Muhammad-Sukki, R. Prabhu, T. Mallick, W. Whittow, S. Kamnis, Thermal spray coatings for electromagnetic wave absorption and interference shielding: a review and future challenges, Adv. Eng. Mater. 24 (2022) 2200171, https://doi.org/10.1002/adem.202200171.

[10] R. Ahmed, O. Ali, C.C. Berndt, A. Fardan, Sliding wear of conventional and suspension sprayed nanocomposite WC-co coatings: an invited review, J. Therm. Spray Technol. 30 (2021) 800–861, https://doi.org/10.1007/s11666-021-01185-z.

[11] N.H. Faisal, R. Ahmed, S.P. Katikaneni, S. Souentie, M.F.A. Goosen, Development of plasma sprayed molybdenum carbide-based anode layers with various metal oxide precursors for SOFC, J. Therm. Spray Technol. 24 (2015) 1415–1428, https://doi.org/10.1007/s11666-015-0315-2.

[12] N.H. Faisal, R. Ahmed, A. Prathuru, S. Katikaneni, M. Goosen, S.Y. Zhang, Neutron diffraction residual strain measurements of molybdenum carbide based solid oxide fuel cell anode layers with metal oxides on Hastelloy X, Exp. Mech. 58 (2018) 585–603, https://doi.org/10.1007/s11340-017-0298-7.

[13] R. Ahmed, N.H. Faisal, A.M. Paradowska, M.E. Fitzpatrick, K.A. Khor, Neutron diffraction residual strain measurements in nanostructured hydroxyapatite coatings for orthopaedic implants, J. Mech. Behav. Biomed. Mater. 4 (2011) 2043–2054, https://doi.org/10.1016/j.jmbbm.2011.07.003.

[14] L. Baoyi, D. Yuping, Z. Yuefang, L. Shunhua, Electromagnetic wave absorption properties of cement-based composites filled with porous materials, Mater. Des. 32 (2011) 3017–3020, https://doi.org/10.1016/j.matdes.2010.12.017.

[15] M. Tului, F. Arezzo, L. Pawlowski, Optical properties of plasma sprayed ZnO+ Al$_2$O$_3$ coatings, Surf. Coat. Technol. 179 (2004) 47–55, https://doi.org/10.1016/S0257-8972(03)00800-4.

[16] R. Vaßen, Z. Yi, H. Kaßner, D. Stöver, Suspension plasma spraying of TiO$_2$ for the manufacture of photovoltaic cells, Surf. Coat. Technol. 203 (2009) 2146–2149, https://doi.org/10.1016/j.surfcoat.2008.10.021.

[17] Y. Gao, J. Xiong, D. Gong, J. Li, M. Ding, Improvement of solar absorbing property of Ni–Mo based thermal spray coatings by laser surface treatment, Vacuum 121 (2015) 64–69, https://doi.org/10.1016/j.vacuum.2015.07.018.

[18] X. Wang, T. Ouyang, X. Duan, C. Ke, X. Zhang, J. Min, A. Li, W. Guo, X. Cheng, Improved solar absorptance of WC/co solar selective absorbing coating with multimodal WC particles, Metals 7 (2017) 137, https://doi.org/10.3390/met7040137.

[19] X. Duan, X. Zhang, C. Ke, S. Jiang, X. Wang, S. Li, W. Guo, X. Cheng, Microstructure and optical properties of co-WC-Al$_2$O$_3$ duplex ceramic metal-dielectric solar selective absorbing coating prepared by high velocity oxy-fuel spraying and sol-gel method, Vacuum 145 (2017) 209–216, https://doi.org/10.1016/j.vacuum.2017.09.002.

[20] Ke, C., Zhang, X., Guo, W., Li, Y., Gong, D-Q., Cheng, X., Solar selective coatings with multilayered structure based on thermal spraying WC-co solar absorption layer. Vacuum, 152, 2018, 114–122. doi:https://doi.org/10.1016/j.vacuum.2018.01.046.

[21] Deng, X-Q., Xue, M-M., Lv, Y-L., Li, R-H., Tong, J-M., Shi, G-H., Yang, Y., Dong, Y-C., Study on spectral selective absorbing coatings with spinel structures fabricated via plasma spraying. Vacuum, 174, 2020, 109214. doi:https://doi.org/10.1016/j.vacuum.2020.109214.

[22] J. Dong, Y. Shi, C. Huang, Q. Wu, T. Zeng, W. Yao, A new and stable Mo-Mo$_2$C modified g-C3N4 photocatalyst for efficient visible light photocatalytic H$_2$ production, Appl. Catal. B Environ. 243 (2019) 27–35, https://doi.org/10.1016/j.apcatb.2018.10.016.

[23] S. Liu, N. Cui, S. Liu, P. Wang, L. Dong, B. Chen, N. Zhang, K. Zhang, Y. Wang, Nonlinear optical properties and passively Q-switched laser application of a layered molybdenum carbide at 639 nm, Opt. Lett. 47 (2022) 1830–1833, https://doi.org/10.1364/OL.454047.

[24] H. Xu, W. Cen, Z. Tian, Q. Zheng, T. Gao, Y. Liang, Q. Quan Xie, A first principles study of the surface electronic properties of Mo$_2$C, Solid State Commun. 353 (2022) 114867, https://doi.org/10.1016/j.ssc.2022.114867.

[25] A. Sinhamahapatra, J.P. Jeon, J. Kang, B. Han, J.-S. Yu, Oxygen-deficient zirconia (ZrO$_{2-x}$): a new material for solar light absorption, Sci. Rep. 6 (2016) 27218, https://doi.org/10.1038/srep27218.

[26] M. Shi, T. Qiu, B. Tang, G. Zhang, R. Yao, W. Xu, J. Chen, X. Fu, H. Ning, J. Peng, Temperature-controlled crystal size of wide band gap nickel oxide and its application in electrochromism, Micromachines 12 (2021) 80, https://doi.org/10.3390/mi12010080.

[27] Costantini, J-M., Cavani, O., Boizot, B., On-line optical absorption of electron-irradiated yttria-stabilised zirconia. J. Phys. Chem. Solids, 169, 2022, 110853. doi: https://doi.org/10.1016/j.jpcs.2022.110853.

[28] F.M. Smits, Measurement of sheet resistivities with four-point probe, Bell Syst. Tech. J. 37 (1958) 711–718, https://doi.org/10.1002/j.1538-7305.1958.tb03883.x.

[29] J. Tauc, R. Grigorovichi, A. Vancu, Optical properties and electronic structure of amorphous germanium, Phys. Status Solidi 15 (1966) 627–637, https://doi.org/10.1002/pssb.19660150224.

[30] P. Makuła, M. Pacia, W. Macyk, How to correctly determine the band gap energy of modified semiconductor photocatalysts based on UV–vis spectra, J. Phys. Chem. Lett. 9 (2018) 6814–6817, https://doi.org/10.1021/acs.jpclett.8b02892.

[31] P. Kubelka, F. Munk, A contribution to the optics of pigments, Z. Technol. Phys. 12 (1931) 593–599.

[32] P.E. Santangelo, G. Allesina, G. Bolelli, L. Lusvarghi, V. Matikainen, P. Vuoristo, Infrared thermography as a non-destructive testing solution for thermal spray metal coatings, J. Therm. Spray Technol. 26 (2017) 1982–1993, https://doi.org/10.1007/s11666-017-0642-6.

[33] Bobzin, K., Wietheger, W., Burbaum, E., The effect of water absorption in ceramic coatings on high frequency AC resistance, Thermal Spray 2021: Proceedings from the International Thermal Spray Conference (ITSC 2021), Paper No: itsc2021p0315, pp. 315–321. doi:10.31399/asm.cp.itsc2021p0315.

[34] J.B. Lee, A.I. Radu, P. Vontobel, D. Derome, J. Carmeliet, Absorption of impinging water droplet in porous stones, J. Colloid Interface Sci. 471 (2016) 59–70, https://doi.org/10.1016/j.jcis.2016.03.002.

[35] ASTM E2109–01 (2021): Standard test methods for determining area percentage porosity in thermal sprayed coatings. https://www.astm.org/e2109-01r21.html.

[36] Lakiza, S., Hrechanyuk, M., Red'ko, V., O.K. Ruban, Ja.S. Tyshchenko, A.O. Makudera, O.V. Dudnik, The role of hafnium in modern thermal barrier coatings. Powder Metall. Met. Ceram., 60, 78–89, 2021. doi:https://doi.org/10.1007/s11106-021-00217-1.

[37] M.L. Montero-Sistiaga, S. Pourbabak, J.V. Humbeeck, D. Schryvers, K. Vanmeensel, Microstructure and mechanical properties of Hastelloy X produced by HP-SLM (high power selective laser melting), Mater. Des. 165 (2019) 107598, https://doi.org/10.1016/j.matdes.2019.107598.

[38] K.A. Habib, D.L. Cano, J.A.H. Alvaro, J. Serrano-Mira, R. Llopis, D. López Moreno, S.S. Mohammed, Effects of thermal spraying technique on the remelting behavior of NiCrBSi coatings, Surf. Coat. Technol. 444 (2022) 128669, https://doi.org/10.1016/j.surfcoat.2022.128669.

[39] J. Wang, J. Sun, H. Zhang, S. Dong, J. Jiang, L. Deng, X. Zhou, X. Cao, Effect of spraying power on microstructure and property of nanostructured YSZ thermal barrier coatings, J. Alloys Compd. 730 (2018) 471–482, https://doi.org/10.1016/j.jallcom.2017.09.323.

[40] M. Naftaly, S. Das, J. Gallop, K. Pan, F. Alkhalil, D. Kariyapperuma, S. Constant, C. Ramsdale, L. Hao, Sheet resistance measurements of conductive thin films: a comparison of techniques, Electronics 10 (2021) 960, https://doi.org/10.3390/electronics10080960.

[41] P. Ctibor, J. Sedlacek, R. Musalek, T. Tesar, F. Frantisek Lukac, Structure and electrical properties of yttrium oxide sprayed by plasma torches from powders and suspensions, Ceram. Int. 48 (2022) 7464–7474, https://doi.org/10.1016/j.ceramint.2021.11.291.

[42] Z. Sun, W. Fan, Z. Liu, Y. Bai, Y. Geng, J. Wang, Improvement of dielectric performance of solid/gas composite insulation with YSZ/ZTA coatings, Sci. Rep. 9 (2019) 3888, https://doi.org/10.1038/s41598-019-40515-8.

[43] M. Watanabe, S. Kuroda, H. Yamawaki, M. Shiwa, Terahertz dielectric properties of plasma-sprayed thermal-barrier coatings, Surf. Coat. Technol. 205 (2011) 4620–4626, https://doi.org/10.1016/j.surfcoat.2011.03.144.

[44] Lin, Y-C., Yen, W. T., Wang, L. Q., Effect of substrate temperature on the characterisation of molybdenum contacts deposited by DC magnetron sputtering. Chin. J. Phys., 50, 2012, 82–88. http://PSROC.phys.ntu.edu.tw/cjp.

[45] L. Li, The advances and characteristics of high-power diode laser materials processing, Opt. Lasers Eng. 34 (2000) 231–253, https://doi.org/10.1016/S0143-8166(00)00066-X.

[46] L. González-Fernández, L. del Campo, R.B. Pérez-Sáez, M.J. Tello, Normal spectral emittance of Inconel 718 aeronautical alloy coated with yttria stabilized zirconia films, J. Alloys Compd. 513 (2012) 101–106, https://doi.org/10.1016/j.jallcom.2011.09.097.

[47] J. Yin, L. Zhang, W. Ma, C. Wang, Q. Zhang, X. Zhang, C. Deng, M. Zhang, X. Weng, L. Deng, Research on reducing infrared emissivity of 8YSZ coating by regulating microstructure, Infrared Phys. Technol. 130 (2023) 104587, https://doi.org/10.1016/j.infrared.2023.104587.

[48] G. Yang, C.Y. Zhao, A comparative experimental study on radiative properties of EB-PVD and air plasma sprayed thermal barrier coatings, J. Heat Transf. 137 (2015) 091024, https://doi.org/10.1115/1.4030243.

[49] M. Radovic, E. Lara-Curzio, R.M. Trejo, H. Wang, W.D. Porter, Thermophysical properties of YSZ and Ni-YSZ as a function of temperature and porosity, Advances in Solid Oxide Fuel Cells II: Ceramic Engineering and Science Proceedings 27 (2006) 79–85, https://doi.org/10.1002/9780470291337.ch8.

[50] Emissivity – Metals. https://www.flukeprocessinstruments.com/en-us/service-and-support/knowledge-center/infrared-technology/emissivity-metals?utm_source=chatgpt.com (accessed January 2025).

[51] J.D. Buckley, Thermal conductivity and thermal shock qualities of zirconia coatings on this gage Hastelloy-X metal, Am. Ceram. Soc. Bull. 49 (1970) 588–591. https://ntrs.nasa.gov/api/citations/19680026296/downloads/19680026296.pdf.

[52] R.K. Maynard, Total Hemispherical Emissivity of Very High Temperature Reactor (VHTR) Candidate Materials: Hastelloy X, Haynes 230, and Alloy 617, University of Missouri, Columbia, 2011. https://ui.adsabs.harvard.edu/abs/2011PhDT.......331M/abstract.

[53] R. Siegel, C.M. Spuckler, Analysis of thermal radiation effects on temperatures in turbine engine thermal barrier coatings, Mater. Sci. Eng. A 245 (1998) 150–159, https://doi.org/10.1016/S0921-5093(97)00845-9.

[54] C. Ungaro, S.K. Gray, M.C. Gupta, Black tungsten for solar power generation, Appl. Phys. Lett. 103 (2013) 071105, https://doi.org/10.1063/1.4818711.

[55] C. Dwivedi, P. Bamola, B. Singh, H. Sharma, Chapter 2 - Infrared Radiation and Materials Interaction: Active, Passive, Transparent, and Opaque Coatings, Editor

(S): Goutam Kumar Dalapati, Mohit Sharma, Energy Saving Coating Materials, Elsevier, 2020, pp. 33–56, https://doi.org/10.1016/B978-0-12-822103-7.00002-9.

[56] J. Anand, D.J. Sailor, A. Baniassadi, The relative role of solar reflectance and thermal emittance for passive daytime radiative cooling technologies applied to rooftops, Sustain. Cities Soc. 65 (2021) 102612, https://doi.org/10.1016/j.scs.2020.102612.

[57] J.H. Henninger, Solar Absorptance and Thermal Emittance of some Common Spacecraft Thermal Control Coatings, NASA Reference Publication 1121, 47 P. https://ntrs.nasa.gov/api/citations/19840015630/downloads/19840015630.pdf, 1984.

[58] B. Ziaeemehr, Z. Jandaghian, H. Ge, M. Lacasse, T. Moore, Increasing solar reflectivity of building envelope materials to mitigate urban heat islands: state-of-the-art review, Buildings 13 (2023) 2868, https://doi.org/10.3390/buildings13112868.

[59] Case Study: Natural Stone Solar Reflectance Index and the Urban Heat Island Effect, Center for Clean Products, The University of Tennessee, 2009. https://www.naturalstoneinstitute.org/default/assets/file/consumers/casestudy4_solarreflectanceofstone.pdf.

[60] C. Yang, C. Wöll, IR spectroscopy applied to metal oxide surfaces: adsorbate vibrations and beyond, Advances in Physics: X 2 (2017) 373–408, https://doi.org/10.1080/23746149.2017.1296372.

[61] M.B. Kakade, K. Bhattacharyya, R. Tewari, R.J. Kshirsagar, A.K. Tyagi, S. Ramanathan, G.P. Kothiyal, D. Das, Nanocrystalline La0.84Sr0.16MnO3 and NiO-YSZ by combustion of metal nitrate-citric acid/glycine gel - phase evolution and powder characteristics, Trans. Indian Ceram. Soc. 72 (2013) 182–190, https://doi.org/10.1080/0371750X.2013.851620.

[62] Z. Wei, H. Qiao, H. Yang, L. Zhu, X. Yan, Preparation and characterization of NiO nanoparticles by anodic arc plasma method, J. Nanomater., Article ID 795928 (2009), https://doi.org/10.1155/2009/795928.

[63] A. León, P. Reuquen, C. Garín, R. Segura, P. Vargas, P. Zapata, P.A. Orihuela, FTIR and raman characterization of TiO₂ nanoparticles coated with polyethylene glycol as carrier for 2-methoxyestradiol, Appl. Sci. 7 (2017) (2017) 49, https://doi.org/10.3390/APP7010049.

[64] M. Al-Amin, S.C. Dey, T.U. Rashid, M. Ashaduzzaman, S.M. Shamsuddin, Solar assisted photocatalytic degradation of reactive azo dyes in presence of anatase titanium dioxide, International Journal of Latest Research Engineering and Technology 2 (2016) 14–21. http://www.ijlret.com/Papers/Vol-2-issue-3/14-B2016126.pdf.

[65] S. Sagadevan, J. Podder, I. Das, Hydrothermal synthesis of zirconium oxide nanoparticles and its characterisation, J. Mater. Sci. Mater. Electron. 27 (2016) 5622–5627, https://doi.org/10.1007/s10854-016-4469-6.

[66] P.J. Lezzi, M. Tomozawa, R.W. Hepburn, Confirmation of thin surface residual compressive stress in silica glass fiber by FTIR reflection spectroscopy, J. Non-Cryst. Solids 390 (2014) 13–18, https://doi.org/10.1016/j.jnoncrysol.2014.02.021.

[67] Wang, G., Sang, S., Wang, Q., Sun, Y., Li, Y., Infrared radiation property and enhancement mechanism of MgCr₂O₄ doped with NiO prepared at different temperature. *Ceramics International*, **50**, Part A, 2024, 9–19. doi:https://doi.org/10.1016/j.ceramint.2023.10.109.

[68] J. Yin, C. Wang, H. Zheng, L. Zhang, M. Zhang, X. Ma, T. Shen, W. Zhang, X. Weng, S. Jiang, X. Zhang, J. Fan, C. Deng, L. Deng, Power controlled microstructure and infrared properties of air plasma spraying based on YSZ coatings, Surf. Coat. Technol. 426 (2021) 127768, https://doi.org/10.1016/j.surfcoat.2021.127768.

[69] S. Heiroth, R. Ghisleni, T. Lippert, J. Michler, A. Wokaun, Optical and mechanical properties of amorphous and crystalline yttria-stabilized zirconia thin films prepared by pulsed laser deposition, Acta Mater. 59 (2011) 2330–2340, https://doi.org/10.1016/j.actamat.2010.12.029.

[70] Yang, G., Zhao, C. Y., A comparative experimental study on radiative properties of EB-PVD and air plasma sprayed thermal barrier coatings. J. Heat Transf., 137, 2015, 091024-12. doi:https://doi.org/10.1115/1.4030243.

[71] P. Amézaga-Madrid, A. Hurtado-Macías, W. Antúnez-Flores, F. Estrada-Ortiz, P. Pizá-Ruiz, M. Miki-Yoshida, Synthesis, microstructural, optical and mechanical

[72] properties of yttria stabilized zirconia thin films, J. Alloys Compd. 536 (2012) S412–S417, https://doi.org/10.1016/j.jallcom.2011.11.111.

[72] J. Yin, L. Zhang, W. Ma, C. Wang, Q. Zhang, X. Zhang, C. Deng, M. Zhang, X. Weng, L. Deng, Research on reducing infrared emissivity of 8YSZ coating by regulating microstructure, Infrared Phys. Technol. 130 (2023) 104587, https://doi.org/10.1016/j.infrared.2023.104587.

[73] Eldridge, J. I., Spuckler, C. M., Street, K. W., Markham, J. R., Infrared radiative properties of yttria-stabilized zirconia thermal barrier coatings, in: 26th Annual Conference on Composites, Advanced Ceramics, Materials, and Structures: B: Ceramic Engineering and Science Proceedings, 2002, pp. 417–430. doi:https://doi.org/10.1002/9780470294758.ch47.

[74] E.J. Gildersleeve, R. Vaßen, Thermally sprayed functional coatings and multilayers: a selection of historical applications and potential pathways for future innovation, J. Therm. Spray Technol. 32 (2023) 778–781, https://doi.org/10.1007/s11666-023-01587-1.

[75] P.A. Giguère, K.B. Harvey, On the infrared absorption of water and heavy water in condensed states, Can. J. Chem. (1956) 798–808, https://doi.org/10.1139/v56-103.

[76] Sun, X., Wang, K., Fan, Z., Wang, R., Mei, X., Lu, Y., Regulation of hydrophobicity on yttria stabilized zirconia surface by femtosecond laser. *Ceramics International*, **47**, Part A, 2021, 9264–9272. doi:https://doi.org/10.1016/j.ceramint.2020.12.053.

[77] Lee, S., Yoon, H., Lee, S., Chung, S. M., Kim, H., Investigation of the hydrophilic nature and surface energy changes of HfO₂ thin films prepared by atomic layer deposition. *Vacuum*, **219**, Part A, 2024, 112756. doi:https://doi.org/10.1016/j.vacuum.2023.112756.

[78] Z. Zhou, Y. Jia, Q. Wang, Z. Jiang, J. Xiao, L. Guo, Recent progress on molybdenum carbide-based catalysts for hydrogen evolution: a review, Sustainability 15 (2023) 14556, https://doi.org/10.3390/su151914556.

[79] Y. He, K. Xiong, E. Xia, Growth of dry patches in an evaporating film flowing around a horizontal circular tube, International Communications in Heat and Mass Transfer 125 (2021) 105291, https://doi.org/10.1016/j.icheatmasstransfer.2021.105291.

[80] M. Bai, M. Kazi, X. Zhang, J. Liu, T. Hussain, Robust hydrophobic surfaces from suspension HVOF thermal sprayed rare-earth oxide ceramics coatings, Sci. Rep. 8 (2018) 6973, https://doi.org/10.1038/s41598-018-25375-y.

[81] Liu, J., Wang, J., Memon, H., Fu, Y., Barman, T., Choi, K-S., Hou, X., Hydrophobic/icephobic coatings based on thermal sprayed metallic layers with subsequent surface functionalization. Surf. Coat. Technol., 357, 2019, 267–272. doi:https://doi.org/10.1016/j.surfcoat.2018.10.002.

[82] N. Ludwig, E. Rosina, A. Sansonetti, Evaluation and monitoring of water diffusion into stone porous materials by means of innovative IR thermography techniques, Measurement 118 (2018) 348–353, https://doi.org/10.1016/j.measurement.2017.09.002.

[83] V. Murali, J.C.H. Zeegers, A.A. Darhuber, Infrared thermography of sorptive heating of thin-porous media – experiments and continuum simulations, Int. J. Heat Mass Transf. 147 (2020) 118875, https://doi.org/10.1016/j.ijheatmasstransfer.2019.118875.

[84] P. Zhao, G.K. Hargrave, H.K. Versteeg, C.P. Garner, B.A. Reid, E.J. Long, H. Zhao, The dynamics of droplet impact on a heated porous surface, Chem. Eng. Sci. 190 (2018) 232–247, https://doi.org/10.1016/j.ces.2018.06.030.

[85] J. Schwede, I. Bargatin, D. Riley, B.E. Hardin, S.J. Rosenthal, Y. Sun, F. Schmitt, P. Pianetta, R.T. Howe, Z.-X. Shen, N.A. Melosh, Photon-enhanced thermionic emission for solar concentrator systems, Nat. Mater. 9 (2010) 762–767, https://doi.org/10.1038/nmat2814.

[86] J. Schwede, T. Sarmiento, V. Narasimhan, S.J. Rosenthal, D.C. Riley, F. Schmitt, I. Bargatin, K. Sahasrabuddhe, R.T. Howe, J.S. Harris, N.A. Melosh, Z.-X. Shen, Photon-enhanced thermionic emission from heterostructures with low interface recombination, Nat. Commun. 4 (2013) 1576, https://doi.org/10.1038/ncomms2577.